HHS Public Access

Author manuscript

J Magn Reson Imaging. Author manuscript; available in PMC 2022 July 01.

Published in final edited form as:

J Magn Reson Imaging. 2021 July ; 54(1): 36–57. doi:10.1002/jmri.27247.

Diffusion imaging in the post HCP era

Steen Moeller[1], **Pramod Kumar Pisharady**[1], **Jesper Andersson**[3], **Mehmet Akcakaya**[1,2], **Noam Harel**[1], **Ruoyun(Emily) Ma**[1], **Xiaoping Wu**[1], **Essa Yacoub**[1], **Christophe Lenglet**[1], **Kamil Ugurbil**[1]

[1]Center for Magnetic Resonance Research; Department of Radiology, University of Minnesota.

[2]Electrical and Computer Engineering, University of Minnesota, Minneapolis, MN, United States

[3]Wellcome Centre for Integrative Neuroimaging, FMRIB, Nuffield Department of Clinical Neurosciences, University of Oxford, Oxford, United Kingdom

Abstract

Diffusion imaging is a critical component in the pursuit of developing a better understanding of the human brain. Recent technical advances promises to enable the advancement in the quality of data that can be obtained. In this review the context for different approaches relative to the Human connectome projects are compared. Significant new gains are anticipated from the use of high performance head gradients. These gains can be particularly large when the high performance gradients are employed together with ultrahigh magnetic fields. Transmit array designs are critical in realizing high accelerations in dMRI acquisitions, while maintaining large FOV coverage, and several techniques for optimal signal-encoding are now available. Reconstruction and processing pipelines that precisely disentangles the acquired neuro anatomical information are established and provide the foundation for the application of Deep learning in the advancement of dMRI for complex tissues.

Introduction

The Human Connectome Project (HCP) was planned and initiated nearly a decade ago as two multi-institutional undertakings aimed at establishing new benchmarks for understanding connectivity in the human brain using neuroimaging. Together, these projects produced exquisite magnetic resonance (MR) imaging data on neuroanatomy, brain responses to a multitude of tasks and/or stimuli mapped by functional imaging (t/sfMRI), structural and functional connectivity derived from diffusion weighted imaging (dMRI), and correlated spontaneous fluctuations captured by “resting state” fMRI (rfMRI), respectively. Over a relatively short period of time, these projects significantly advanced the instrumentation as well as image acquisition, reconstruction, and analysis methods in pursuit of developing a better understanding of the human brain “connectome” (i.e. the organization and interaction of structural and functional networks), much like the Human Genome

Corresponding author Steen Moeller, Ph.D., Center for Magnetic Resonance Research, University of Minnesota, 2021 6th Street SE, Minneapolis, MN, 55455, USA, moeller@cmrr.umn.edu.

Projects, (HGP, 1990–2004), or the NIH Advanced Sequencing Technology Development (ASTD, 2004–2013) propelled efforts towards unveiling our genetic blueprint (the genome).

Of the two multi-institutional initiatives, the WU-Minn Consortium (with primary participants Washington University in St. Louis, University of Minnesota, and Oxford University) was responsible for generating a large, 1200 subject imaging database obtained at 3 Tesla (3T), complemented with genetic and behavioral measures across subjects (1). A smaller database was also generated at 7 Tesla (7T) (2,3), using ~180 individuals from the 1200 subject pool of the 3T database. Following an approximately three-year period focused on advancing hardware, image acquisition, data collection protocols, and image analysis pipelines, the WU-Minn consortium established a new imaging standard for large population studies (e.g. (1,4–8)). The 3T component of this major effort included dMRI acquisitions that utilized three shells with b=1000, 2000, 3000 s/mm^2 exploiting a gradient set with high maximal strength of 100 mT/m. The number of shells and the b values employed were decided upon subsequent to extensive technical developments and piloting on subjects similar to the targeted population (6,7).

The second HCP initiative, the MGH-USC Consortium, focused almost exclusively on establishing a unique 3T instrument with 300 mT/m maximal gradient strength (G_{max}) specifically for dMRI, and generated a 35 subject dMRI data set using a 4 shell acquisition, with b=1000, 3000, 5000 and 10000 s/mm^2 (9); the significantly higher G_{max} of this instrument permitted the use of b values greater than 3000 s/mm^2.

Achieving substantial accelerations was a central target in the WU-Minn Consortium and this was attained through slice acceleration using simultaneous multi-slice (SMS)/multiband (MB) approach for the 3T and using both slice and phase encoding accelerations in the 7T components of their effort. In contrast, MGH-USC consortium, acquiring data at 3T, only relied on acceleration along the phase encode direction (Table 1). There were other major differences in the 3T dMRI acquisition parameters of the two different consortia: For example, nominal resolution was 1.25 mm isotropic in the WU-Minn data (7), whereas it was 1.5 mm isotropic in the MGH-USC effort (Table 1); this difference, together with the choice of accelerations led to different TRs and TE's in the two databases (TR/TE= 5900/89 ms for WU-Minn (7) and 8800/57 ms for MGH-USC (Table 1)). These projects have been previously reviewed and described in detail (1,4,6–10).

The avalanche of transformative technologies that were brought together in the HCP for neuroimaging in general, and for diffusion and functional imaging in particular, provided the motivation to adapt these technologies by many other large-scale projects. This was also catalyzed by the early, well-supported, and well-documented public availability of the HCP methods (e.g. the image acquisition and reconstruction methods from the University of Minnesota, Center for Magnetic Resonance Research (CMRR) for SMS/MB technique (https://www.cmrr.umn.edu/downloads/), correction and image analysis methods from FIMRIB in Oxford (https://fsl.fmrib.ox.ac.uk/fsl/fslwiki/FSL), and analysis and visualization platform from Washington University in St. Louis (https://www.humanconnectome.org)), and recent commercialization of the acquisition techniques by MR vendors. At the very least, the success of the original HCP carried out on a young adult population has led

to three new HCP projects focused on the human Lifespan (Baby Connectome) (11), HCP-Lifespan-Development (12), HCP-Lifespan-Aging (13) and numerous Disease Connectome projects (see https://www.humanconnectome.org for a list); these projects are focused on collecting HCP style data using the methods developed and made available by the WU-Minn consortium. The lessons learned from the HCP are similar to those that could be learned from the genome mapping project (14), namely: *1. Aggressively encourage technology development from; the start; 2. Consider practical applications from the start; 3. The goal need not be "simple." 4. Lack of prior "understanding" should not impede innovation.*

dMRI is currently the only imaging method available to map short and long-range brain pathways *in vivo* (for recent collections of reviews see special issue volume edited by Alexander Leemans et al. (15)). Although this technique was the subject of transformative refinements within the HCP, achieving further substantial advances should remain a major research focus since significant inaccuracies remain in tracing connections in the human brain with dMRI based tractography. A recent global tractography challenge (16), based on a high-quality HCP data yielded a general consensus that 90% of the well-known axonal bundles could be correctly determined; however, the same tractograms (i.e. sets of tractography outputs) also contained a substantial number of false positive bundles, and half of these invalid bundles occurred systematically across the efforts undertaken by the different research groups. Moreover, assessment of the volumetric extent of these pathways was only about one-third accurate (i.e. 30% spatial agreement). Taken together, these results highlight persisting fundamental limitations that justify major efforts in seeking considerable new improvements in dMRI in the post HCP era, pursuing higher signal-to noise ratios (SNR), higher spatial resolution imaging, faster k- and q-space sampling, and superior tractography algorithms. Such pursuits are the subject matter of this review article, and are presented in 6 sections covering the MR signal (signal magnitude, SNR efficiency, multi-shell and TE choices), the MR system (gradients, and receive and transmit arrays), the image reconstruction algorithms, pre-processing pipelines, Q-space sampling and biological systems modelling, and imaging techniques different from the HCP approach.

MR Signal and Mono Polar EPI for Diffusion Encoding.

Both HCP projects selected mono-polar spin-echo Echo Planar (SE-EPI) approach that employs a single, nominally 180°, refocusing pulse for dMRI to maximize the acquired signal. This approach amplifies the magnitude of the deleterious eddy currents induced by the diffusion gradients. In addition, single shot k-space encoding by EPI acquisition suffers from off-resonance effects due to B_0 inhomogeneities as well as the eddy currents that may persist onto the EPI readout period. Thus, rigorous methods for correcting eddy-current (17), and off-resonance effects (18) had to be developed. Viable alternatives such as STEAM-dMRI (19) for diffusion contrast were considered, particularly for high magnetic fields, but ultimately rejected due to the 2-fold SNR loss suffered in stimulated echoes.

SE-EPI Signal Magnitude and SNR efficiency

The signal S for SE-EPI (20), is described as [Eq. 1]

$$S = M_0 \sin(\theta_{EX}) \sin^2(\theta_{ref}/2) \left)\frac{1 + (\cos(\theta_{ref}) - 1) e^{\left(-\frac{(TR - TE/2)}{T_1}\right)} - \cos(\theta_{ref}) e^{\left(-\frac{TR}{T_1}\right)}}{1 - \cos(\theta_{ref}) \cos(\theta_{EX}) e^{\left(-\frac{TR}{T_1}\right)}} e^{\left(-\frac{TE}{T_2}\right)} \right. \quad \text{[Eq. 1]}$$

where θ_{EX} and θ_{ref} are the excitation and refocusing flip angles respectively, and TE, T_1, and TR are the relevant MR parameters. S gives amplitude the signal for the center of k-space. However the rest of the points during the EPI readout will be affected by T_2 and T_2* decay, and this effect is in addition to [Eq. 1]. The signal behavior under diffusion is reflective of the underlying tissue and commonly assessed with a single diffusion encoding (21), such that

$$s(b) = s(0) e^{-bD} \quad \text{with} \quad b = (\gamma \delta |\boldsymbol{g}|)^2 \left(\Delta - \frac{\delta}{3}\right) \quad \text{[Eq. 2]}$$

where γ is the gyromagnetic ratio, $\boldsymbol{g}$ the gradient vector defined from the magnetic field gradient, δ the gradient pulse length, Δ the diffusion time between gradient pulses and D the diffusivity. Of course, D is a scalar in a homogeneous medium but is a tensor in complex structures like the brain. Analysis of the SE-EPI signal using [Eq. 1], can elucidate that the signal is maximized for long TR, with a 180° refocusing pulse ($\sin^2(\theta_{ref}/2)$), and that the signal dependence on TE is dominated by an exponential decay model ($e^{\left(-\frac{TE}{T_2}\right)}$).

In terms of defining optimal acquisition parameters, the concept of SNR efficiency, defined as SNR/√TR, is introduced since a shorter TR leads to larger number of scans within a total acquisition period and hence to improved SNR due to increased averaging while at the same time leading to decreases in SNR due to incomplete relaxation. For a 90° excitation and 180° refocusing pulses, and TE/T_1=65ms/1200ms the relative SNR efficiency (independent of the $e^{(-TE/T_2)}$ term in Eq. 1) is plotted as a function of TR in Figure 1A; this is the source of the frequently expressed notion that the SNR is maximized at a TR of 1.2×T_1 (22) for a spin-echo sequence with a single refocusing pulse. At TR's longer than the optimal TR, SNR efficiency decreases slowly with increases in TR. Given that white matter T_1 is ~900 ms at 3T and ~1200 ms at 7T (23), the optimum TR for a dMRI acquisition using a single refocusing pulse would be ~1 to ~1.5 s for 3T and 7T, respectively, and somewhat longer at higher magnetic fields. Because of the broad maxima in this SNR efficiency curve, one can even tolerate TR's of ~2.5 s before significant degradation begins to occur. Achieving such TRs for *high resolution imaging* is highly challenging in whole brain studies due to the large amount of data that needs to be collected (i.e. large number of slices and k-space points needed for each slice). The delay period TE imposed by the diffusion encoding also adds to the challenge of reducing TR. Consequently, the HCP dMRI data were obtained with repetition times far away from this optimal TR range, ranging from 5500 ms in the 3T component of the WU-Min HCP (7) to 8900 ms in the MGH-USC consortia (Table 1). The HCP Lifespan, where the dMRI resolution is 1.5 mm isotropic and 4-fold slice acceleration is employed, achieves a shorter TR (3200 ms) (Table 1) (12), which is still longer than the optimal TR.

Thus, TR and volume acquisition times (VAT)[1], which are the same in a slice based imaging approach, are suboptimal in the HCP; reducing this parameter towards the optimal value requires both reducing TE and increasing image accelerations, irrespective of the imaging approach used, whether slice based as in the HCP or segmented 3D EPI or spiral trajectory acquisitions (e.g. (20,24–26)) that are gradually being explored as an alternative. This in turn requires major new developments in hardware as well as image acquisition and reconstruction strategies, which are increasingly a major focus of the post HCP era in the development of dMRI as well as fMRI techniques.

MR Systems

Pursuit of Shorter TE using High Performance Gradients

For a multi-shell dMRI, such as those used in the HCP projects, diffusion modelling pre-supposes the use of the same TE for all shells; this TE is determined by the highest b value, which penalizes the SNR for lower shells. In the case of the young adult HCP, the SNR loss due to fixed TE is plotted in Figure 1B for the WU-Minn consortium data, showing that as much as 16% signal loss is encountered for the b=1000 s/mm^2 shell when the TE is set by the b=3000 s/mm^2 shell. This SNR reduction is further aggravated due to the diffusion weighting itself, which inherently decreases the measured signal with increasing b values (Figure 1C). Consequently, dMRI studies aiming for high resolution and/or carried out at high magnetic fields, employ relatively low diffusion weighting, such as b=1000 s/mm^2 or less, and only one shell (e.g. (27–29)). While such low b values do permit the construction of some fibers through tractography which may look pleasing to the eye, they are significantly suboptimal with respect to capturing multiple fiber crossings (6).

Therefore, developments towards achieving relatively high b values with short TEs as well as TR's that optimize SNR remain a critical need in the post HCP era. The dominant determinant of the TE is gradient performance. Hence, the drive towards establishing high performance gradients in the HCP naturally continues in the post HCP era.

HCP Gradients—SNR in a dMRI acquisition strongly depends on gradient performance. During the delay time TE where diffusion encoding takes place, the MR signal decays exponentially with T_2 leading to SNR losses (Eq. 1). For a given b-value, decreasing the duration of the diffusion gradients by increasing their amplitude and slew rates reduces the TE and increases the SNR. Therefore, the two original young adult HCP efforts used modified custom gradient systems, as previously mentioned. The connectome scanner for the MGH-USC project was a 3T Siemens Skyra outfitted with a custom gradient set that achieved a G_{max} of 300 mT/m with a slew rate of 200 T/m/s when driven by 4 Siemens Aera gradient amplifiers. The scanner for the WU-Minn project was also a 3T Siemens Skyra; this instrument was outfitted with the SC72 Siemens gradient coil normally used on the 7T Siemens scanners, and driven by a single Aera gradient amplifier to achieve G_{max} of 100 mT/m and 200 T/m/s slew rate. The WU-Minn HCP project also had a 7T

[1]Note that while TR and volume acquisition time (VAT) are the same in a slice based imaging approach, this is not the case in segmented 3D imaging where k-space is sampled in 3 dimensions. For the latter, TR is used as the time between two consecutive RF pulses exciting the same spatial volume (e.g. slice or slab) and TR<<VAT.

component, which employed a standard Siemens 7T instrument equipped with the SC72 Siemens gradient coil driven by an Avanto gradient amplifier to achieve 70 mT/m gradient-strength and 200 T/m/s slew rate. At the time, commercial 3T instruments typically provided maximal gradient strength of ~40 mT/m with 200 T/m/s slew rate.

None of the gradient sets available in clinical or connectome scanners could fully utilize the slew rates the hardware can achieve. They were all limited by peripheral nerve stimulation (PNS) and, in case of the two 3T connectome gradients, also by cardiac stimulation. Especially the G_{max}=300 mT/m connectome set encounters the cardiac limitation since this limit is kicked in at approximately 100 mT/m (9,30). At the hardware slew rate limit, the 300 mT/m can be reached in 1.5 ms; with the cardiac limitation, it takes ~6 ms to achieve it (9,30), thus diminishing the impact of the high G_{max} values for decreasing the TE in diffusion encoding. Nevertheless, the high maximal strength HCP gradients operating in 3T scanners clearly provided significant SNR gains for dMRI acquisitions compared to what was available at the time (6,9).

For the two HCP gradients, the similar slew-rates up to ~100 mT/m imply that for low b-values the two systems yield similar SNR in dMRI, while for high b-values the stronger gradients permit shorter TEs thus retaining more image SNR, despite having to employ slower slew rates. The calculated relative SNR gain between the two systems are shown in Figure 1D for a b-value less than and equal to 3000 s/mm^2 for different maximal gradient strengths without taking into account the slew rate (i.e. assuming infinitely fast slew rate) (7). Similar calculations were provided in (4). Experimental gains in reducing the TE and increasing SNR were shown for the 300 mT/m gradient set of the MGH-USC consortium scanner (9) illustrating major improvements especially for high b- values of 10,000 or 20,000 s/mm^2; such high b-values are not practical even for the G_{max}= 100 mT/m Connectome gradient, but achievable with a G_{max} of 300 mT/m despite the slower slew rates that must be employed in reaching that maximal strength, yielding numerous advantages in dMRI based tractography or microstructure determination (e.g. see review (30)).

Head only Gradients—Overcoming the slew rate limitation at the present requires head only gradient systems (31–34) and/or possibly new designs that take into account PNS in defining the gradient wiring (35). The higher slew rates have an additional significant benefit besides their contribution to achieving high b values; namely they allow smaller echo-spacings in fast acquisition schemes like EPI and spiral trajectories that are employed in dMRI, further contributing to SNR gains, and suppression of off-resonance distortions and blurring. Among the recent efforts, a head-only 42 cm internal diameter (ID) gradient designed for a compact 3T system achieves 80 mT/m peak gradient amplitude with a slew rate of 700 T/m/s on each gradient axis using readily available 1-Mega Volt-Amp (MVA) gradient drivers (34). It is able to achieve similar diffusion encoding as the WU-Minn HCP system, benefiting from the higher slew rate to reduce TE despite the slightly lower G_{max} relative to the WU-Minn HCP scanner. A smaller, 33 cm ID, head gradient developed so as to fit into the bore of whole body MR system was reported to achieve 100 mT/m and 1200 mT/m/s when driven by 720 Amp/1300 Volt amplifiers (31) and has been employed in dMRI scans with TE= 19 ms at b=1000 s/mm^2 (36). At the present time, in projects funded by the NIH's BRAIN Initiative (U01 EB025144 and U01 EB025162) towards establishing

next generation human neuroimaging platforms, high performance head only gradients are also being pursued in industrial-academic collaborations, aiming for ≳100 mT/m maximal strength with ≳700 T/m/s slew rate.

When evaluating and comparing the G_{max} and slew rate performance of head gradients, it is critical to keep in mind that the gradient performance depends strongly on the gradient driver amplifiers used, which have been increasing in current and voltage over the years, the size of the gradients, particularly the ID which strongly influences the achievable G_{max} per unit current, the shielding efficiency, the volume over which linearity is desired, and the degree of the linearity over that volume, which impacts particularly the slew rate. It will be interesting to see what kind of compromises will emerge in the on-going efforts to substantially improve performance using head gradient designs. Actual achievable performance in a real dMRI experiment will also depend on additional considerations. Most importantly, thermal performance and eddy currents induced in the magnet will be critical. The latter can lead to temperature rises in the magnet, which can have catastrophic consequences. The former is critical for contemporary developments in neuroimaging, particularly functional and diffusion weighted imaging, which push for ever-higher accelerations in data acquisition; such acceleration gains will often be used to sample more data points per unit time while keeping the total acquisition time still relatively long. This means that the gradients must attain very high G_{max} and slew rates using high currents and voltages at increasingly high duty cycles over long periods of time.

An interesting aspect of the BRAIN Initiative funded projects pursuing new head gradients is that they are associated also with ultrahigh fields (UHF) like 7T or 10.5T. The advantages of the high gradient slew rates in k-space encoding at very high magnetic fields is clear. Namely, at high B_0 fields, magnetic field inhomogeneities, and shorter T_2* and T_2 become a bigger challenge for rapid acquisition schemes like EPI and spiral, especially when implemented as single-shot trajectories. Faster slew rates, hence faster rate of covering k-space, alleviates this problem. However, these projects also target major gains in dMRI.

dMRI and UHF

Among many practitioners of dMRI, there is the concept (may be even better called a “prejudice”) that UHF is inherently disadvantageous for dMRI. This is true in the limit that TEs employed for diffusion encoding are long compared to T_2; in this limit, the intrinsic SNR advantage of the ultrahigh magnetic field such as 7 or even 10.5T will be lost due to the shorter T_2 and hence faster longitudinal relaxation and signal loss during TE. However, as TE’s become smaller, the losses associated with the shorter T_2 at the higher magnetic fields are not sufficient to negate the intrinsic SNR gain available at the higher magnetic field (7). This was shown early on for reduced FOV diffusion weighted single-shot SE-EPI with 50–100% SNR improvements at 7T relative to 3T (37); however, this SNR gain was limited without access to current scan-efficient techniques, and high gradient strengths. In particular, SNR gain could not be extended to whole-brain imaging in the absence of SAR and B1 management tools, which are now available (38).

The long TE regime for diffusion encoding, which is disadvantageous for ultrahigh magnetic fields, was applicable especially in the early days of dMRI when typically two refocusing

pulses and bipolar gradients in three intervals between the excitation radio frequency (RF) pulse and data acquisition were employed for diffusion encoding. This was done in order to counteract and minimize the eddy current effects (39). However, with eddy current distortion corrections becoming feasible in the HCP (40), or through the use of field monitoring (41,42), a move to a single refocusing pulse together with the use of high performance gradients, as employed in the HCP, have already shortened TEs where ultrahigh fields actually provide net gains in dMRI.

This was demonstrated in the WU-Minn young adult HCP consortium, where dMRI data were obtained on the same 180 subjects at both 3T and 7T instruments. This unique dataset showed distinct advantages for the 7T: The 7T dMRI data was obtained with 1.05 mm vs. 1.25 mm isotropic nominal resolution used for the 3T acquisitions, which corresponds to ~2 fold smaller voxel volumes at 7T. The real voxel volume calculated by taking into account the point spread function was even smaller for the 7T where the echo train lengths were kept short by using undersampling in the phase encode direction (2,43). The 3T dMRI used a G_{max}= 100 mT/m as previously mentioned while the 7T only had 70 mT/m for G_{max}; as such, the 7T was handicapped from the point of view of gradient performance. Despite this, the 7T data had unique advantages with respect to gyral bias (43). At the time, it was decided in the WU-Minn consortium that, because of the lower gradient performance, the b=3000 s/mm^2 shell that was employed on the 3T dMRI would not be used for the 7T dMRI data. However, subsequently, it was demonstrated that the addition of this shell still has enough SNR to provide information and leading to a 7T dMRI data acquired using the same 3 shells employed in the 3T HCP protocol (44). An example from this 3-shell 7T effort is shown in Figure 2.

Higher Resolution using UHF—The performance of tractography is reduced when there is an ambiguous correspondence between diffusion directions and fiber geometry (e.g. crossing, divergence). Often the focus has been on the crossing fiber problem in white matter; however, accurately following fibers becomes a major problem also at the boundary between white and gray matter where fibers can sharply turn from the white matter into the gyral wall and subsequently penetrate the cortical laminae where radial and tangential fibers coexist. This makes it challenging to completely track the end-to-end connections for creating joint structural and functional connectomes. In this respect, the 2-shell 7T HCP data was already significantly better than the 3-shell 3T HCP data due its higher spatial resolution, but further significant improvements were achieved when the three-shell 3T HCP protocol was also applied at 7T while keeping the spatial resolution at 1.05 mm isotropic (44). This is demonstrated by tractography streamlines progressively bending into and penetrating the cortex (Figure 2) not only toward the gyral crown but also throughout the walls. Such UHF results demonstrating improved tractography relative to 3T HCP data of course would attain further major gains with enhanced gradient performance which was not been available for these 7T data.

Thus, significant new gains are anticipated for dMRI in the post HCP developments that will rely on the use of high performance head gradients, particularly large when these high performance gradients are employed together with ultrahigh magnetic fields. The use of high resolution and high magnetic fields also increases the complexity of the problem;

for example, the effect of the coupling between endogenous local field gradients and exogenously applied gradients may become significant as local gradients, which arise from magnetic susceptibility difference at the interface between different tissues, increase in magnitude as B_0 increases. However, the impact from such local gradients also decrease in the presence of large exogenously applied gradients. Since high gradient strengths are needed to fully exploit the SNR advantages UHF for dMRI, this problem would be naturally minimized. However, there are other problems encountered at 3T and particularly at much higher magnetic fields that challenge dMRI acquisitions; some solutions to these problems have been already demonstrated as discussed in the next section; improving upon these solutions and bringing them to easy and routine use will likely be one of the major goals of the superior dMRI acquisitions in the post HCP era.

RF-coils: Receive Arrays

High Channel Receive Capability at 3T—The number of receive channels in the RF coils employed in MRI acquisitions impact SNR and acceleration significantly. In the original HCP, a standard, Siemens 3T 32 channel receive (Rx) head coil was employed for data collection in the WU-Minn consortium and a custom build 64 channel Rx array (45) was used in the MGH-USC consortium.

In clinical 3T systems, vendor supplied 64 channel Rx coils typically do not focus on the "brain" *per se* but rather cover a larger volume as "head and neck" coils; consequently, such 64 Rx "head and neck" coils do not necessarily provide an advantage over the brain compared to a 32 Rx coil that focuses only on the brain. This is the reason why the initial WU-Minn HCP effort and all current HCP projects that are carried on Siemens Prisma scanners employ a vendor supplied 32 Rx coil rather than the available 64 Rx coil from the same vendor.

Approximately 32 Rx channels is expected to capture most of the ultimate intrinsic SNR (uiSNR) available at the center of the brain, as suggested by calculations in a sphere approximating the brain (46). However, higher channel coils improve the peripheral SNR (47), though this increase is expected to be relatively small at 3T compared to higher magnetic fields because, with the smaller coils that must be employed in high density arrays, thermal noise in the coil and associated electronics rather than the sample is expected to dominate (46). Thus, one can argue that there is little to be gained for neuroimaging at 3T for the much larger effort needed when going to channel counts much higher than ~32; this would be true for *unaccelerated* imaging. However, virtually all contemporary imaging and certainly contemporary dMRI relies on some sort of acceleration as previously discussed; consequently such images suffer from noise amplification from the mathematical algorithm used to resolve aliased signals (i.e. the g-factor noise (48)). In this case, using a 64 channel "brain" coil at 3T as employed in the MGH-USC HCP consortium (9) would be highly advantageous, providing reduced g-factor noise, including and especially in the center of the brain, thus increasing SNR (9,49).

High Channel Receive Capability for UHF—In particular, the HCP 7T dMRI studies could have benefited significantly from going beyond 32 channel Rx capability, for example

to 64 or even higher number of Rx channels. However, such a capability was not available at the time. The primary aim of UHF efforts has always included improved spatial resolution (e.g. (50–52)), which adversely impacts volume acquisition times and hence SNR efficiency. The remedy for this problem is higher accelerations, for example in the slice direction in multislice based brain coverage. This was the reason SMS/MB was introduced for brain imaging to begin with, so as to simultaneously excite multiple slices and acquire the combined signal of these slices in the same duration as a single slice, thus aiming for whole brain fMRI with thin slices (i.e. higher resolution) with improved SNR efficiency (53). In addition, increased B_0 inhomogeneities at this ultrahigh magnetic field requires undersampling in the phase encode dimension in order to keep echo train lengths short in techniques like single-shot EPI or spiral trajectories that are commonly used in dMRI and fMRI; this is obligatory for minimizing image distortions, blurring, and signal drop outs in the acquired images. Therefore, in the 7T SMS/MB accelerated dMRI and fMRI imaging in the HCP, undersampling in the phase encode direction by a reduction factor (R) of 3 and 2, respectively, was employed together with slice acceleration (7), resulting in total two dimensional acceleration of MBxR. In this case, unaliasing capability of the receive array employed is challenged not just by the slice acceleration factor of MB, but the total two-dimensional acceleration of MBxR, which at any given field strength will be limited by the number of elements in the Rx array.

Thus, high Rx channel counts are more imperative at UHF. Synergistically, high channel Rx arrays also perform much better at ultrahigh magnetic fields (46,54,55). At 7T and higher, a 96 channel “brain” array composed of relatively small coils employed to achieve such a high channel density is expected to operate in a domain where the sample noise still dominates, capturing a larger fraction of the available uiSNR in superficial voxels (46). While the number of channels greater than 32 are not expected to (46), and do not (49), improve SNR in the center of the brain in *unaccelerated* imaging even at 7T, they are expected to improve SNR in the entire brain, including the center in the highly *accelerated* dMRI acquisitions required for 7T.

However, the unavailability of greater than a 32 channel *receiver* system at 7T at the time of the young adult HCP, precluded using a higher than 32 Rx coil, even a home-built one. This was a major limitation. Eliminating this limitation has been one of the major goals of development in the post HCP era, not only for dMRI, which is the subject of this review, but also for fMRI.

The afore discussed improvements expected at 7T with arrays greater than 32 elements was recently demonstrated (49). In the fMRI component of the young adult HCP, MBxR = 5×2 acceleration was employed. Going beyond that resulted in unacceptable g-factor noise with the 32 channel Rx coil used. However, with a 64 channel “brain” coil at 7T, collecting images in the same oblique orientation of the HCP, supported 6×2, 7×2, and even 8×2 accelerations (49) without exceeding the g-factor noise level of the 5×2 HCP data (49). Gains with the 64 Rx coil in the canonical axial, sagittal and coronal orientations are illustrated in Figure 3 as 1/g-factor maps calculated in the whole brain but presented as a MIP on a central sagittal slice (49), showing that if sagittal or coronal slices are employed, 5×3 and even 6×3 fold accelerations would be feasible with the 64 channel coil whereas 32

channel coil would not support greater than approximately 4×3. It is important to note that the performance of both coils are worst with axial slices.

RF Coils: Transmit Arrays

The selection of RF pulse-profile for the excitation and refocusing pulses in the SMS SE-EPI impacts the TE, slice-resolution, saturation of adjacent slices, and spatial distribution of SNR within slices and throughout the volume of interest. In the original WU-Minn HCP, the Siemens optimized 90°−180° pulse-pair, which are a windowed Sinc pulse with a time-bandwidth product of 3.2 for excitation, and 5.2 for refocusing, were employed. This pair of balanced pulses are short, analytic, compatible with the construction of multibanded pulses in SMS/MB, and provide an empirical balance between slice-profile and low power demand (see the (56) for a review of other pulse choices).

Flip Angle (In)homogeneity—The sensitivity of the signal in a SE-EPI sequence to the excitation flip angles is shown in Figure 4a as a function of TR, for the same T_1 value of 1200 ms; the refocusing flip angle was set to 180° to maximize the signal irrespective of the excitation flip angle. The TR employed in the Lifespan HCP, young-normative WU-Minn HCP at 3T and at 7T, and MGH-USC HCP (Table 1) are also indicated on this plot. It is clear that for the TRs achieved in all of these HCP protocols, SNR and SNR efficiency would be highly dependent on the flip angle. However, the flip angle in the human head is not uniform even at 3T but particularly at 7T (Figure 4b and 4c). This nonuniformity exists even with RF transmit coils that would achieve a highly uniform B_1 field in the absence of the head. It is an intrinsic property of the dimensions of the head relative to the wavelength of the RF employed (50,57) and arises from the fact that at 3T and higher fields, the system is increasingly operating in the traveling wave regime (50,57,58). Any coil imperfections of course adds on to this intrinsic inhomogeneity.

At 3T, using the whole body RF transmit coil, there is an ~15% spatial variation (Coefficient of Variation (COV)) in flip angle over the brain; for the 7T acquisition, a single transmit head coil was used, along with di-electric padding, to reduce the C.O.V. to 20% (Figure 4c) with certain regions (e.g. cerebellum and the temporal lobes) having a larger local drop in achievable transmit efficiency (2). The deleterious effects of these transmit B_1 and consequently flip angle inhomogeneities become particularly pronounced in a spin-echo sequence as employed in dMRI where application of the multiple pulses compounds the effect. Thus, the HCP data and, for that matter, virtually all dMRI data obtained at 3T and higher field strengths reported to date also suffer from spatially non-uniform SNR and SNR efficiency within the brain due to *transmit B_1 inhomogeneities*, leading even to regions where tractography fails (2,38).

In the WU-Minn young adult and the Lifespan HCPs, steps were taken to alleviate this problem. With the 32 channel receive array used in these studies, deeper parts of the brain have the lowest receive SNR. Therefore, in order to increase the lowest SNR in the 3T HCP a 90°/180° excitation/refocus were selected for the deeper parts of the brain, which was achieved using average whole brain flip angles of 78°/160°. These problems were partially

improved in the 7T component of the WU-Minn HCP using dielectric pads (2). However, these steps provide only partial mitigation.

Power Deposition Limitations—When the goal is to increase SNR efficiency through faster image acquisition, there is another problem encountered associated with transmit B_1 and RF pulses, particularly in spin echo sequences, namely power deposition in the subject (i.e. specific absorption rate (SAR)). This imposed a limit of MB 3 for the 3T component of the WU-Minn young adult HCP; although in some subjects slightly higher MB factors were possible without violating the SAR limit, HCP stayed with a conservative value of 3 to accommodate the variation that was anticipated in the large number of people scanned in this consortium. The SAR limitation becomes more severe at higher magnetic fields. The 7T dMRI component of the young adult HCP, restricted MB to 2 because of SAR; this enabled the use of a higher phase-encoding undersampling rate of 3, resulting in a 6-fold 2-dimensional acceleration compatible with the unaliasing performance of the 32Rx coil employed. However, the minimum TR achievable with this low MB factor and the larger number of slices needed to accommodate the higher resolution was 7700 ms, which is highly inefficient for SNR.

pTx Design and High Channel Capability—The two problems of flip angle non-uniformities and SAR limitation in accelerated dMRI can be tackled simultaneously by the use of multichannel transmit coils and parallel transmit (pTx) pulses, which can be designed explicitly to reduce power deposition as well as improve flip angle uniformity (38,59–61). Alternative strategies based on the use of relatively low power RF refocusing pulses have also been suggested for ameliorating the SAR problem in UHF dMRI acquisition ((62) and references therein); however, in such approaches, the bandwidth of the refocusing pulses are reduced significantly. This is problematic especially at UHF where B_0 inhomogeneities are inherently large.

The pTx approach is applicable for the MB pulses employed in the SMS/MB based dMRI (63,64). This allows significantly improved flip angle uniformity thus improving spatial SNR uniformity over the brain. Equally important is the ability to use a higher MB factors due to the lower SAR achieved with pTx pulses; this decreases VAT (hence TR in slice based imaging), and improves SNR efficiency. This latter gain can be exploited in different ways. It can be used to decrease the total data collection time given k- and q-space sampling scheme (38). This is an important consideration especially for imaging with young subjects and patients where motion or tolerance of long scan times is more of a problem. Alternatively, the total acquisition time can be kept constant but a larger number of q-space points can be acquired, potentially improving the tractography accuracy.

A full solution using parallel transmission (pTx) was demonstrated at 7T (38); the attainable increase in SNR uniformity that resulted in improved tractography are illustrated in Figure 5 (reproduced from (38)) which shows that particularly the cerebellum and temporal lobe areas (indicated by the arrows in the figure) suffer from the B_1 non-uniformity. In addition, it was demonstrated that higher MB factors can be achieved before SAR limits were reached, even when conservative SAR limits were imposed (38) for safety considerations. With that solution, the experimental SNR-efficiency of MB3 would be ~5% higher due to the shorter

TR, and for MB4 relative to MB3 a further gain of 5% could be realized. Even the 3T data can be improved with pTx in a similar fashion. The theoretical SNR efficiency of the 90°/180° SE-EPI which is optimal TR=1.2×T_1 can be closely maintained over a wider range of roughly 0.8×T_1 to 2×T_1, shown in Figure 4a, and the use of pTx can be applied to balance fewer q-space samples with higher SNR and more q-space samples - each individual sample with low SNR but collectively similar SNR.

Further improvements in alleviating the SAR limitation while simultaneously increasing the flip angle uniformity can be achieved by using higher number of transmit channels, different transmit coil array configurations than those employed in the study by Wu et al (38), and using advanced SAR modeling. Wu et al (38) employed an 8 channel transmit version of the RF coil used in the 7T component of the young adult HCP in order to make direct comparisons; the transmit channels in this coil are azimuthally distributed in a single ring. However, simulations have demonstrated that larger number of transmit channels and distributing the transmit channels in multiple rows along the z direction provides significantly better performance for local, and global SAR mitigation while improving flip angle uniformity (59,61).

Thus, transmit array designs are also critical in achieving high accelerations in dMRI acquisitions. Therefore, compared to the single channel transmit employed in all of the HCP studies to date, significant improvements are possible in acceleration by using optimized multichannel transmit arrays and pTx pulses. However, increased acceleration enabled in this way requires, in addition, a high performing receive array in order to handle the increased aliasing. This is possible with increasing the number of Rx channels as previously discussed and demonstrated with the afore mentioned 64-channel Rx array at 7T (49)(Figure 3). This 7T 64 channel Rx array was in fact designed with a 16 channel transmitter laid in two rows of eight azimuthally distributed channels along the z-direction with this consideration in mind (49); this initial foray into 16 transmit (Tx)/64 Rx at 7T (49) likely will be overtaken by RF coils operating with up to 32 Tx and up to 128 Rx or more channels in the future and such coils will become a critical part of post HCP dMRI data acquisition. These developments will be critical for surpassing the already excellent HCP dMRI data in the post HCP era.

Image Reconstruction with Slice and Phase-Encode Accelerated Imaging

Controlled Aliasing with SMS/MB

The use of parallel Imaging in the HCP was imperative for increasing the SNR efficiency. As previously discussed, acceleration along both slice and/or phase encoding dimensions were employed. At the time of the young adult HCP, the GRAPPA reconstruction for parallel imaging data was mature, but the SMS/MB acquisition needed to be further improved for encoding and reconstruction.

Exciting slices simultaneously and afterwards unaliasing them with parallel imaging reconstruction was first introduced in 2001 (reviewed in (56)). The performance of this approach was subsequently improved with the CAIPIRINHA (Controlled Aliasing in Parallel Imaging Results in Higher Acceleration) technique (reviewed in (56)) for unaliasing

of simultaneously excited slices imaged with a Gradient Recalled Echo (GRE) (also referred to as FLASH) acquisition scheme where a single k-space line is acquired after each RF pulse; in this approach, the slices were shifted relative to each other by using a slice specific modulation of RF pulse phases exciting the spins before each k-space line. Such an approach is not possible with EPI acquisition. Instead, CAIPIRINHA using a constant slice-encoding gradient blip between EPI k-space lines was introduced in 2006 so as to impose a slice specific phase modulation superimposed on phase encoding (reviewed in (56)). However, the constant slice-encoding blip scheme produced a dephasing within the slice in the slice direction.

SMS/MB for EPI

Subsequent to these efforts, development of EPI based slice acceleration stalled, probably because of lack of an immediate application that would highly benefit from these developments. Such an application was first introduced for high resolution fMRI at 7T (53). This effort did not use CAIPIRINHA encoding along the slice direction; it introduced also the first demonstration of acceleration along the phase encode axis simultaneously with slice acceleration, achieving 16-fold two-dimensional acceleration. The enthusiasm generated with this early brain application led to additional developments for encoding and unaliasing. The CAIPIRINHA encoding for EPI was changed from a constant slice-encoding blip scheme to a balanced slice-encoding blip scheme termed “blipped-CAIPI” (65), aiding unaliasing without the within-slice dephasing of constant slice encoding.

The undersampling of k-space for accelerating in the phase encoding dimension results in the Field of View (FOV) folding (i.e. aliasing) onto itself. For slice acceleration in SMS/MB where the FOV is not undersampled *per se*, the simultaneously excited slices appear summed or overlaid in the image domain; if SMS/MB is thought of as a 3D acquisition (66), then the FOV can also be thought of as folding (i.e. aliasing) onto itself. This latter approach was taken in the original, highly accelerated brain implementation (53), an approach referred to as readout (RO)-SENSE-GRAPPA. An alternative strategy termed Slice-GRAPPA (65) was subsequently introduced and was shown to have better g-factor noise performance than RO-SENSE-GRAPPA at high acceleration factors. Because of this, Slice-GRAPPA was adapted for the young adult HCP. Both slice-GRAPPA, and RO-SENSE-GRAPPA are compatible with the deterministic GRAPPA g-factor calculation (67). For slice-GRAPPA, noise-decorrelation needs to be applied prior to calculating the g-factor, whereas for RO-SENSE-GRAPPA it can be used either way as described in (67).

Performance of Reconstruction Algorithms

The g-factor parallel imaging performance of the slice-GRAPPA approach was evaluated (68) and, differently from phase-encoding parallel imaging, it did not have more than a linear increase in noise-amplification from increased undersampling; in other words, g-factor noise alone was inadequate to assess the performance of the unaliasing of the simultaneously excited slices in SMS/MB. This necessitated the concept of slice leakage (L-factor) as a new metric (68) for differentiating the performance of SMS/MB by measuring residual aliasing among the simultaneously excited slices.

Subsequently, improvements to the slice-GRAPPA algorithm was proposed to reduce the slice leakage, using an additional constraint for kernel calibration in slice-GRAPPA, an approach termed Split Slice-GRAPPA (Sp-Sg) (69), introducing the concept of "slice blocking". The Sp-Sg reconstruction has higher g-factor noise compared to slice-GRAPPA; however, it is significantly more advantageous with respect to leakage among simultaneously excited slices (70). Consequently, slice-GRAPPA, which was chosen over RO-SENSE-GRAPPA in the original young adult HCP because of its superior g-factor noise suppression, was abandoned for Sp-Sg, which has inferior g-factor characteristics (Figure 6) but less interslice leakage.

The concept of "slice blocking" for reducing slice-leakage is not used in conventional parallel imaging with phase encode undersampling; it is purely a concept necessitated by the implementation of slice-GRAPPA, which turns out to be suboptimal. Both GRAPPA and RO-SENSE-GRAPPA use shift invariant convolutional kernels for data interpolation and the kernels are calibrated from a Nyquist sampled reference data using all possible patterns. In Slice-GRAPPA, the kernels are used as projection operators and calibrated from individually acquired single slice data. The slice-GRAPPA approach proposed in (65) determines the projections kernels as the mapping of *"the sum of the individual slices to the individual single band"*; had either the Minnesota or the MGH group implemented this as the calibration of the "*sum of any complex combination of the individual slice to the individual slice"*, the concept of slice-blocking would not have been needed. Referring to the implementation of slice-GRAPPA using this formulation as "unbiased slice-GRAPPA", one can write,

$$\begin{aligned} &\boldsymbol{G}_j\left(\sum_i S_i\right) = S_j \quad \forall j && \text{[A: Slice-GRAPPA]} \\ &\boldsymbol{G}_j\left(\sum_i S_i\right) = S_j \quad \forall j \; AND \; \boldsymbol{G}_j(S_i) = 0, i \neq j && \text{[B: Sp-Sg]} \\ &\boldsymbol{G}_j\left(\sum_i \alpha_i S_i\right) = S_j \quad \forall j \quad \forall \alpha_i \text{ with } |\alpha_i| = 1 && \text{[C: Unbiased Slice-GRAPPA]} \end{aligned} \qquad \text{[Eq. 3]}$$

As a linear system, *any complex combination* can be implemented using the basis function for the complex Hadamard Transform such that for an MB factor of N, the linear system to determine the unbiased slice-GRAPPA is N times larger than for determining the slice-GRAPPA kernel. With this formulation Sp-Sg, Unbiased slice-GRAPPA and RO-SENSE-GRAPPA, are equivalent in performance (71) with respect to both g-factor noise and interslice leakage, and superior to the original slice-GRAPPA.

Next Generation of Algorithms

Thus, in the post HCP era, at least we have a better and a unifying understanding of the reconstruction algorithms for SMS/MB acquisitions. The reconstruction algorithms will continue to be a critical part of post HCP dMRI, as the number of channels and the degree of undersampling are increased. Recent advances in linear reconstructions with Virtual coils (72) and kernel regularization (73) have improved the conditioning of the interpolation by reducing the propagation of noise from the measurements, and promises to enable better utilization of the data. Finally, recent advances in non-linear deep learning (DL) reconstructions (74) are poised to provide additional benefits for

reconstruction. One of the main challenges for application of DL in diffusion MRI remains the lack of fully-sampled reference data with which to perform supervised training. This challenge is being addressed in different ways. One line of work considers database-free methodologies, where convolutional neural networks trained on ACS data are used to improve k-space interpolation (75). These methods have also been shown to improve the noise and artifact reduction for SMS imaging at high acceleration factors in fMRI (76). Another line of work considers self-supervised database-based training from undersampled data only (77). This method works with so-called physics-driven neural networks, where an optimization algorithm for solving a regularized inverse problem is unrolled for a fixed number of iterations, and then trained end-to-end. These methods hold promise for even higher acceleration rates due to the regularizers built into them (78). Their application to diffusion MRI faces several challenges due to the high number of input channels to the neural network, which includes all diffusion weightings per slice, and thus warrants further investigation.

Preprocessing Pipelines for HCP Diffusion MRI

The move to a single refocusing pulse in the HCP projects instead of the conventional bipolar gradient design increased the sensitivity to eddy current-induced fields that distort the k-space trajectories of the single-shot SE-EPI employed for acquiring the k-space data; this perturbation comes in addition to the distortions in the SE-EPI acquisition caused by the off-resonance frequency shifts induced by susceptibility gradients within the target imaged. The local geometric distortions are estimated and corrected by minimizing the sum-of-squared differences between two acquisitions with reversed phase-encoding that induce opposing distortions, an approach that is referred to as the TOPUP technique (18). The off-resonance field just above the sinuses in the human brain in a typical subject is ~150Hz at 3T. For the dMRI acquisition with an echo-spacing of 0.78 ms, nominal phase-encoding resolution of 1.25mm and phase-encoding FOV of 210mm, the maximal susceptibility-induced off-resonance shift is ~8 pixels (5% of the FOV). This distortion is within the capability of TOPUP. For correcting subject movement effects and the eddy current-induced off-resonance fields, a rigid body movement model and a 3D static second order polynomial model for the eddy current-induced off-resonance field were used for the initial cohort of HCP data, referenced as the EDDY technique (79). The predictive data model in EDDY, using a Gaussian process built for TOPUP, also facilitates detecting movement-induced signal drop out by comparing the observed to the predicted total signal in each slice. In the HCP implementation of EDDY, outlier slices were replaced by the model predictions in this way, thus ensuring that they have a minimal impact on subsequent analysis. The predictive data model in the Gaussian process ensures a multi-dimensional solution that is a consistent discrete sampled solution of a continuous and smooth model both on and between q-space shells.

Continuous Motion Model and Dynamic Susceptibility Map

The eddy current-induced off-resonance field correction method continued to be developed following the conclusion of the original HCP project. The volumetric rigid body model employed in the original HCP breaks down when movement is fast, relative to the repetition

time. An extended predictive model allows EDDY to include a continuous motion model within a repetition time such that each slice can have a unique rigid body model with a continuous parameterization of the motion relative to their temporal sampling (80). In the case of large, though not necessarily rapid, subject movement one encounters another problem. The first approximation that the susceptibility-induced off-resonance field, i.e. the disturbance of the field caused by the object/head follows the subject, no longer holds. This has been solved by estimating, directly from the data and with no additional measurements, "rate of change maps" that specify how the field changes as a consequence of rotation in every part of the brain (10). The attainable improvements are illustrated in Figure 7 reproduced from this work. In Figure 7, the left column shows the impact on whole brain consistency with a rigid versus a continuous model; in the center and right column, the difference between a static and a dynamic susceptibility map is shown for two different q-space vectors (top and bottom row), showing how with the dynamic susceptibility map the volumes are consistently aligned across different diffusion contrasts (i.e. on the right most column, the two images corresponding to the two different q-vectors are consistent with each other in distortions (but of course not contrast; this is not the case for the static susceptibility map based correction).

Short TR Confound for Motion

The HCP provided a new way of rapidly acquiring copious amounts of data from a large cohort of subjects. This was aided by the new methods for handling and correcting subject movement and non-linear eddy current-induced fields. One, as of yet unsolved, problem with shortening the TR is that it increases the sensitivity to movement induced spin history effects, and how to correctly account for these in post-processing is not yet established. In practice increasing the SNR efficiency through shortening of the TR is balanced against a related decrease in tSNR which directly affects the parameter estimation. This is further exasperated when fewer q-samples are used which reduces the data redundancy for the predictive data model in EDDY to perform the estimation of eddy current fields and dynamic susceptibility mapping while simultaneously detect and correct for movement-induced signal drop outs. When within TR motion is present, some of the spins will get excited more than once within the TR period due to the movement or some may not get excited at all within the TR but get excited later by the RF pulses coming for the next volume acquisition. For long TRs, the signal is still close to fully relaxed and these effects will not introduce "spin history" effects. For the 5500ms TR in the HCP, assuming T_1=1200ms, the signal is 99% relaxed. In the presence of motion (considering just within TR motion and interleaved slice ordering), if the same spins are acquired earlier relative to the TR, e.g. TR/2=2800ms, the spins are only 91% relaxed and induce a different signal change than the one modelled with changing q-space sampling. For the Lifespan HCP, with a shorter TR=3500ms, the signal is 94% relaxed and possibly 76% relaxed if motion reduces the effective TR to TR/2=1800ms. The relative signal change due to motion in this case is larger than for the long TR choice, 24% and 10% for the short and long TR, respectively, but the likelihood of within TR motion is also reduced with shorter TR's and maximizing SNR efficiency with less than fully relaxed signals is balanced against increased complex signal fluctuations.

It was noted in the HCP data that the slices associated with the first one or two groups of simultaneously excited slices are less than optimally corrected for eddy currents. This is caused by long time-constant eddy currents, which means that the eddy current induced field from the diffusion gradient employed for one volume extends into the next volume. Since multiple slices throughout the head are simultaneously excited and experience the same diffusion encoding gradient in acquisitions with SMS/MB, these long time-constant eddy currents effect slices based on their sequence of excitation with the MB pulses rather than, for example, in a linear fashion going from the basal slices to the superior slices, where only the basal slices would be most affected.

Alternative to the post-acquisition correction of EDDY approach is field monitoring (81) and using the data to correct the k-space trajectories directly for the eddy-current induced field perturbations (e.g. (42,82)). This alone would not correct for motion effects. The motion can still be corrected in addition by EDDY or incorporating motion tracking and prospective adjustments during acquisitions (e.g. (83,84)). Although the feasibility of these technologies and potential improvements have been demonstrated, their robust and routine incorporation into dMRI acquisitions remains to be accomplished. This may represent one of the major efforts that can impact significantly how dMRI is acquired in the post-HCP era.

Q-space Sampling

The ability to acquire large amounts of data, using the tools developed by the HCP, also triggered the need to assess the relevance of the content of such data, and to decide what information should be acquired in q-space. In the HCP, the quality of fiber orientation mapping and tractography results was selected as the overarching guide for protocol optimization. For fiber orientation mapping, BedpostX (85,86) was employed as the primary analysis method, but the data was acquired to be compatible also with various other methods, dictating matched TE and TR across b-values. Once the fiber tracking is done, the quality of dMRI series is evaluated using the number of second and third fibers (i.e. 2- or 3-way fiber crossings) resolved (6).

Inference across the candidate acquisition options demonstrated that a single low to medium b-value was sufficient for second fiber detection only, but that low b-value in combination with high b-values was necessary to resolve 3-way crossings; in such a multi shell (i.e. multi b-value) diffusion encoding, the difference between shells had to be larger than 750 s/mm^2 to significantly aid in third fiber detection. These guidelines and experimental evaluations performed with pilot data supported a proposed 3-shell acquisition in the young adult WU-Minn HCP with b= 1000, 2000, 3000 s/mm^2 and Δb=1000 s/mm^2 (6); because of the shorter total scan times needed in the Lifespan HCP, the dMRI acquisition employed two shells with b equal to 1500 and 3000 s/mm^2, which were chosen based on further evaluation (12). The attainable crossing detection sensitivity across different q-space sampling patterns are illustrated in Figure 8.

Modelling the Signal

A variety of “multi-compartment” (also called biophysical) models have been proposed in the past 10–15 years, that aim to capture more accurately the variability of the

diffusion signal in the intra-axonal and extra-axonal compartments (21). In particular (see (87) for references), these models directly provide information about the white matter microstructure. They include ball-and-stick, CHARMED (composite hindered and restricted model of diffusion), AxCaliber, ActiveAx or the Minimal Model of White Matter Diffusion (MMWMD), NODDI (Neurite Orientation Dispersion and Density Index) and DIAMOND. The CONNECT project recently leveraged the CHARMED, AxCaliber and ActiveAx models to improve structural connectivity mapping methods. Parameter estimation in these biophysical models requires complex non-convex optimization, even for a single axonal orientation, and new techniques such as MIX (87).

Besides these modeling and computational considerations, diffusion acquisition parameters must also be adapted to capture the diffusion properties of pools of water molecules under different regimes (e.g. hindered or restricted diffusion), thereby probing tissue environments (e.g. axons with different diameters) more comprehensively. For example, the density and diameter distribution of axons in a white matter pathway determine its information-bearing capacity; different densities, shapes and configurations of cells discriminate between different types of brain tumor; widespread protein deposits are hallmarks of Alzheimer's disease. The stronger gradient hardware has enabled the use of a broader range of range of b-values with reasonably short TE, leading to a broader range of effective diffusion imes ($\Delta - \frac{\delta}{3}$) with short diffusion pulse time δ. Specifically, while assuming the narrow pulse approximation ($\delta \ll \Delta$), optimized feasible acquisition protocols with |G|=200mT/m (animal system), as opposed to 70mT/m (human system), have been proposed and shown to accurately capture axonal radii at 5 and 10 μm and, to some extent, at 1,2, and 20 μm (88). Nonetheless, despite these improvements, estimating axonal diameters from diffusion MRI data below about 2 μm is still challenging and diffusion experiment optimization for microstructure mapping is still an important and challenging research topic (21). Indeed from the recent review (21) the biophysical models underpinning current microstructure imaging techniques remain crude and a variety of anomalous results point to the fact that the design choices steering the acquisition protocols are oversimplifications of the underlying micros structure environment. In support of this, with the advent of slice accelerated techniques, the improved efficiency of q-space sampling has extended the acquisition design choices including the acquisitions of multiple shells with high angular resolution in feasible scan times. Furthermore, combining this efficiency with the increased dynamic range of the sampling of diffusion times, afforded by the large gradient amplitudes, allows for an increased opportunity to probe tissue microstructure in humans and support more complex bio-physical models.

Solving the Model of the Signal

In addition the extraction of information from dMRI data can be performed by a variety of probabilistic and dictionary-based methods and algorithms (89) such as BedpostX (85), which is a fully probabilistic framework for estimating local probability density functions of parameters of interest from a model of diffusion. It was recently extended and generalized to leverage information from data acquired at multiple spatial resolutions (RubiX) (90). In this multiresolution data fusion algorithm, a lower resolution but high SNR "prior" dataset is combined with higher resolution but lower SNR dataset using a Bayesian model to estimate

the fiber parameters at the highest measured resolution. This approach also enhances the reproducibility of fiber estimation while relaxing the q-space sampling criteria without a linear “SNR” loss.

In BedpostX, automatic relevance determination (ARD) is used to accurately recover fiber orientations supported by the data during the data-driven parameter estimation process. The parameters (e.g. fiber volume fractions) that are not supported by the data will have value zero with very low variance in the posterior distribution. This relevance determination was recently further enhanced in BusineX (91) through relevance learning by tuning the variance prior hyperparameters individually (e.g. locally) and independently for each possible fiber orientation. Furthermore, in the BusineX framework, the exponential decay components along different possible diffusion directions is exploited to construct an overcomplete dictionary with the volume fractions of fibers along these directions defining the dictionary weights. The estimation of fiber parameters is then formulated as a sparse signal recovery problem and a linear unmixing framework with sparse Bayesian learning used for the recovery of sparse signals i.e. the fiber orientations and associated volume fractions.

A dictionary approach such as BusineX is more robust under q-space undersampling, similar to the application of compressed sensing in q-space (92). As an illustrative example for a sample dataset from the WU-Minn HCP, the fiber orientations at pons are reproduced in Figure 9 with color coded orientation estimates (orientation distribution functions in the case of CSD). Here, the background is the sum of anisotropic volume fractions for BusineX and BedpostX, and fractional anisotropy (FA) for the CSD - the measures for resolving the fiber structures. Furthermore in Figure 9, bottom right, the sensitivity under q-space undersampling is plotted for BedpostX (dashed lines) and BusinesX (solid lines) using the number of two (blue) and three-way (red) fiber crossings detected, illustrating how data-dependent local learning of hyperparameters, at each voxel and for each possible fiber orientation, can improve the parameter extraction.

Deep learning-based methods (93) for extracting structural information from diffusion weighted signals have very recently started to be developed. The ability to extract more accurately the variability of the diffusion signal from large data-sets (here demonstrated with BusineX and shown in Figure 9) is one reason that DL models will be further advanced and used to extract even more information than what can easily be described with conventional techniques. Recent studies report accurate DTI reconstruction (94) and fiber orientation distribution function (95) reconstruction, using neural networks, which promise to improve tractography even in complex tissue geometry areas and demonstrate the extraction of increased information from existing data. DL based reconstruction methods have also shown the ability to generate images for Diffusion Kurtosis Imaging (DKI) and NODDI model with less data (96), and the transition from these retrospective analysis to prospective analyses will elucidate the applications that will require larger amounts of data or will perform well with less data, and from which more information can be obtained. For most biophysical models, the optimal protocol is empirically determined; while the training of DL makes its application more protocol specific than existing solvers, the development and validation of a protocol that will support a multitude of biophysical models warrants further investigation.

Imaging Techniques Different from 2D SMS/MB

Although both HCP projects selected a mono-polar, 2D,single-shot SE-EPI based SMS/MB approach for volume encoding, there are plausible alternatives, which independently continue to be advanced. The proposed extensions from Cartesian 2D single-shot EPI for k-space sampling and volume encoding are: multi-shot 2D or 3D EPI, and 2D or 3D single or multi-shot non-Cartesian trajectories such as spiral. Depending on their implementation, these alternative approaches can provide higher SNR through shortened TE, reduced point spread function (PSF), and reduced distortion of images (before pre-processing) through reduced echo-spacing or encoding of the T_2* decay, and commonly considered independent of the earlier discussed TR related optimal SNR efficiency.

In this context we will describe some of the SNR performances of more advanced and typically multi-shot techniques, specifically readout segmented EPI, phase encode segmented EPI (MUSE and IRIS), Hadamard slab encoding (gslider), 3D-EPI, and non-Cartesian acquisitions (for their relative merits we refer to the recent review by Holdsworth et al (19)). A common problem that needs to be addressed in all the segmented multi-shot acquisitions is the *inconsistency* of the phase at the end of diffusion encoding, the “diffusion phase” that commonly arises from motion induced B_0 field variations around the refocusing pulse. These need to be corrected with either navigators (26,97) or data-driven (98,99) approaches. Additionally, the magnitude inconsistencies from the previously discussed spin history effects are mostly ignored and integrated implicitly as an averaging effect such that shorter TR’s can be utilized.

Phase Encoding Segmented Techniques,

The techniques referred to as aMUSE/MUSE/MUSSEL combine phase-encoding segmented acquisitions by using the diffusion-phase difference between the segments. The SNR of these segmented techniques are similar to the scan-time matched single-shot 2D-EPI without slice acceleration, since the gain in SNR from shortening of the TE is offset by the multiple repetitions, and the reduction in geometric distortion is equal to the number of segments. For N>2 the VAT is longer than for the single-shot 2D-EPI, and if the off-resonance blur has not been reduced enough, acquisitions with opposite PE-directions may still be necessary. The MUSSEL technique combines the highly segmented acquisition using a low-rank constraint for the phase-variation among shots. aMUSE/MUSE is a two-step reconstruction with first estimating the phase and then performing a SENSE optimal recombination and reconstruction. The k-space equivalent to aMUSE is with a realigned GRAPPA reconstruction (see Holdsworth et al (19)) where the GRAPPA weights are approximating both the missing data and the phase-variations.

Readout Segmented Techniques,

By only acquiring a smaller amount of the frequency-encoded signal, the echo-spacing in an EPI readout can be reduced. For example with RESOLVE, 3–7 blades are typically used, and each covers a blade in k-space acquired with some overlap. The readout is typically a sinusoidal gradient such as to not exceed peripheral nerve stimulation. The inefficiency of sinusoidal readouts relative to a trapezoidal gradient results in a 50% longer echo-spacing

for comparable k-space coverage, such that the reduction in geometric distortion is not equal to the number of blades. The shorter readout furthermore decreases scan efficiency, which is reduced less with the sinusoidal readouts. The reconstruction of the segments with different diffusion-phases is augmented with a separately acquired navigator, which increases the TR by ~30% depending on resolution (see Holdsworth et al (19)). As such the longer than minimal echo-spacing increases the SNR of readout segmented techniques by using a bandwidth that is lower than the bandwidth for either 2D EPI or the phase-encoding segmented acquisitions, and the ETL balances the SNR efficiency against the geometric distortions.

Hadamard Techniques,

Prior to SMS, the use of Hadamard encoding (see the review (56)) for simultaneously acquiring non-adjacent slices was proposed as one option for extending the FOV. In Hadamard encoding, the same slices are acquired multiple times and each successive acquisition uses a different phase-relationship between the slices, enabling the separation of individual slices - using N equations with N unknowns. This was recently used for diffusion imaging (100) in the spinal cord and is also the basis for gSLIDER. With gSLIDER, adjacent slices are excited simultaneously and all slices are simultaneously refocused (19,101), with (typically) 5 slices resolved per slab and repeated as many times as there are slices. For excitation, different RF pulses are used for each of the repetitions, each providing a unique phase-relationship between adjacent slices that enables the slices to be subsequently resolved in post-acquisition processing. To improve the consistency of the segmented acquisition, a data-driven phase-correction is combined with a regularized inversion of the segmented system for resolving the slices in each slab.

The potential improvements with these techniques rest on how well the slice boundaries can be defined with RF pulses exciting adjacent slices with different phases.

3D SE-EPI

The use of a 3D acquisition was considered for the MGH-USC consortium but it was not mature enough (9) and had more challenges than single-shot 2D SE-EPI based SMS/MB. In 3D SE-EPI (22) and 3D SE-EVI the volume is covered by one or more slabs, and each slab is resolved into multiple slices using phase slice-encoding. In 3D SE-EPI, k-space data for a single phase-encoding plane, k_x-k_y plane, is acquired after each RF excitation (although this can be further segmented as well), whereas in 3D SE-EVI k-space data in more than one phase encoding plane is obtained for each RF excitation; typically with much longer readouts than what is feasible for dMRI. In this respect, 3D SE-EVI is not compatible with high resolution imaging and will not be discussed further.

The TR in these 3D acquisitions are defined as the time between successive pulses that excite the same volume. Thus, TR is not necessarily equal to VAT as previously discussed, and can be set for optimal SNR by selecting the number of slabs times the time to obtain one readout per slab. Typically, and especially when high resolutions are desired, each slab cannot be fully encoded in 3D in a single shot; instead multiple repetitions are necessary to encode each slab. The volume acquisition time (VAT) is then the TR times the number of

excitations necessary to encode each slab. As such, the volume acquisition time is longer for the 3D SE-EPI relative to an SMS/MB accelerated 2D SE-EPI acquisition. A single image in 3D SE-EPI has sqrt(N) higher SNR than a single 2D SE-EPI image where N is the number of RF excitations needed to encode each slab. For example when, after each RF pulse, a single k_x-k_y plane is acquired, then N is the number of RF excitations needed to encode k_z. However, when matching the volume-acquisition time, the achievable SNR between 2D and 3D become comparable for whole brain coverage with resolutions > $(1mm)^3$, since in this regime the SMS technique is able to obtain TR's in the 3–5 second range and the variation in SNR with TR is slow at the optimal TR (Figure 4). If however, significantly higher accelerations become feasible through the development of higher transmit and receive RF coils, as discussed previously, then the differences between 3D multi-slab and 2D SMS/MB would become even smaller with respect to SNR

For segmented 3D SE-EPI (slice, phase or readout segmented) the diffusion phase (22) is an additional confound that has to be accounted for, in order to obtain stable image quality, and the effect of segmented acquisitions can also reduce the temporal SNR (tSNR) such that gains in SNR are offset (102). An example of the SNR gains possible for resolutions $\ll(1mm)^3$ between 3D and 2D acquisitions are shown Figure 10, and the images in SNR units are shown across a range of VATs enabling direct comparison.

Non-Cartesian Acquisitions

Spiral trajectories for k-space coverage are the most common and efficient non-Cartesian acquisitions alternative to EPI sampling (103). The challenges of spiral compared to EPI (104) are *resonance offset contributions*, *gradient deviations*, and *concomitant field* effects. Advances in spiral acquisitions were, for a long time, challenged by the *unavoidable instrumental inadequacies*, such as defining accurate trajectories with gradients and subject specific static B_0 variations which induces blurring in spiral trajectories. In the more recent review (103) on spiral fMRI, increases in ability to measure activation was summarized, including references for advances for diffusion and perfusion MRI. All of these approaches continued to be combined with the plethora of other advances in MRI, some of which are discussed herein.

The Hahn-echo for a single-refocused SE is formed at a point in time which is equal to twice the interval between the excitation and refocusing pulses. In dMRI acquisitions, k=0 point in k-space is arranged to occur typically at this point in time. When spiral trajectories are employed, a low resolution spiral-in trajectory is played out before acquiring the Hahn-echo at k=0 with a spiral out trajectory. The spiral-in acquisition can be used as a navigator or for combining with the spiral out acquisition. This increase the TE and reduces some of the efficiency of spiral acquisitions (26). Nevertheless, under appropriate instrumental conditions circumstances, spiral trajectories can provide advantages with respect to SNR. As an example, listed in Table 2, are the expected changes in SNR from the shortened TE with single shot spiral versus EPI for three different resolutions, Lifespan resolution, highest before readout gradient mechanical resonance, and lowest past readout gradient mechanical resonances.

The *gradient deviations* were originally corrected by mapping *a priori* the trajectory using pre-scan mapping(105,106) of the gradient response and more recently by correction of the gradient response (see (107) and references therein). With field monitoring or pre-mapping technique, the non-ideal gradient waveform in spiral imaging can be taken into account, yielding a more accurate estimation of concomitant field while correcting off-resonance effects resulting from eddy currents and trajectory deviation (108).

From the HCP data, and as discussed above for EDDY, for ensuring anatomical consistency in dynamically acquired data, the "*static off-resonance*" correction for brain imaging needs to be updated dynamically to ensure that temporally distinct volumes are anatomically consistent.

Thus for spiral imaging with long readouts to be used for obtaining images with high spatial fidelity suitable for detailed parcellation of minute brain organization, the reconstructions optimized to overcome the blurring from the static B_0 also needs to account for the gradient deviations, while also being sufficiently sensitive to estimate and adjust for dynamically changing susceptibility fields over a large range of signal-to-noise ratios.

Noise Variance Reduction

In the HCP projects, a conservative and mostly unbiased approach to data processing was used for evaluation. Recent advanced in conservative noise variance reduction (NVR) techniques have demonstrated how time-series data can be pre-processed to improve the model based fit (109). Specifically for the method referred to as MPPCA (109), the data is modeled as having a low-rank representation with additive Gaussian noise. This theoretical model is used in MPPCA to develop a practical algorithm compatible with diffusion weighted DICOM images. The same small volume of interest (VOI) is used from each volume in a dMRI series, and rearranged into a 2D Cassorati matrix. The singular value decomposition on the Cassorati is calculated and a threshold is applied on the spectrum of the singular values. The threshold is determined based on the distribution of the singular values from a series with noise only; such that signal that cannot be differentiated from noise is removed. In MPPCA, the threshold is calculated from the spectrum itself, in the PCA decomposition it is selected empirically, or it can be selected based on the thermal noise level. Both MPPCA and related approaches finds that a ~2X decrease in statistical fitting error is achievable with appropriate selection of the thresholding. In Figure 11, an example from applying the MPPCA to the $(1.5mm)^3$ resolution Lifespan data with 98 directions is shown; with a b=3000 s/mm^2 image illustrating the noise removal on any individual volume, and the FA illustrating that spatial fidelity is maintained by only removing signal that cannot be distinguished from noise.

Thus, in the post HCP era, a focus in denoising to improve tractography without blurring the effective resolution will be a major advance in dMRI. These denoising efforts will also have a major impact on other MR imaging sequences, such as anatomical and functional imaging.

Summary

Diffusion imaging post HCP will, in the short term, use the same techniques developed for the HCP. The WU-Minn HCP produced data of higher quality, resolution and amount, than what is currently being acquired in large cohorts. The MGH-USC produced data with higher diffusion contrast (high q-space) than what is currently being obtained, and provided a small database for evaluating what high diffusion contrast can provide. However, a combination of innovations in hardware for diffusion weighting, spatial encoding, and transmit B_1 management, and progress in sequence design, strategies for k-space coverage, image reconstruction, pre-processing and post processing will enable significant advances in the achievable spatial and q-space resolution and/or total scan duration in dMRI. However, it will require a supported development and dissemination effort to translate these into routine use, as accomplished in the HCP.

Acknowledgement:

Grant funding P41 EB027061, U01-EB025144

REFERENCES

1. Van Essen DC, Smith SM, Barch DM, Behrens TE, Yacoub E, Ugurbil K, for the WU-Minn HCP Consortium. The WU-Minn Human Connectome Project: An overview. Neuroimage 2013;80:62–79. [PubMed: 23684880]
2. Vu AT, Auerbach E, Lenglet C, Moeller S, Sotiropoulos SN, Jbabdi S, Andersson J, Yacoub E, Ugurbil K. High resolution whole brain diffusion imaging at 7T for the Human Connectome Project. Neuroimage 2015;122:318–331. [PubMed: 26260428]
3. Vu AT, Jamison K, Glasser MF, Smith SM, Coalson T, Moeller S, Auerbach EJ, Ugurbil K, Yacoub E. Tradeoffs in pushing the spatial resolution of fMRI for the 7T Human Connectome Project. Neuroimage 2017;154:23–32. [PubMed: 27894889]
4. Van Essen DC, Ugurbil K, Auerbach E, Barch D, Behrens TE, Bucholz R, Chang A, Chen L, Corbetta M, Curtiss SW, Della Penna S, Feinberg D, Glasser MF, Harel N, Heath AC, Larson-Prior L, Marcus D, Michalareas G, Moeller S, Oostenveld R, Petersen SE, Prior F, Schlaggar BL, Smith SM, Snyder AZ, Xu J, Yacoub E, Consortium WU-MH. The Human Connectome Project: a data acquisition perspective. Neuroimage 2012;62(4):2222–2231. [PubMed: 22366334]
5. Smith SM, Vidaurre D, Beckmann CF, Glasser MF, Jenkinson M, Miller KL, Nichols TE, Robinson EC, Salimi-Khorshidi G, Woolrich MW, Barch DM, Ugurbil K, Van Essen DC. Functional connectomics from resting-state fMRI. Trends Cogn Sci 2013;17(12):666–682. [PubMed: 24238796]
6. Sotiropoulos SN, Jbabdi S, Xu J, Andersson JL, Moeller S, Auerbach EJ, Glasser MF, Hernandez M, Sapiro G, Jenkinson M, Feinberg DA, Yacoub E, Lenglet C, Van Essen DC, Ugurbil K, Behrens TE, for the WU-Minn HCP Consortium. Advances in diffusion MRI acquisition and processing in the Human Connectome Project. Neuroimage 2013;80:125–143. [PubMed: 23702418]
7. Ugurbil K, Xu J, Auerbach EJ, Moeller S, Vu AT, Duarte-Carvajalino JM, Lenglet C, Wu X, Schmitter S, Van de Moortele PF, Strupp J, Sapiro G, De Martino F, Wang D, Harel N, Garwood M, Chen L, Feinberg DA, Smith SM, Miller KL, Sotiropoulos SN, Jbabdi S, Andersson JL, Behrens TE, Glasser MF, Van Essen DC, Yacoub E, Consortium WU-MH. Pushing spatial and temporal resolution for functional and diffusion MRI in the Human Connectome Project. Neuroimage 2013;80:80–104. [PubMed: 23702417]
8. Glasser MF, Smith SM, Marcus DS, Andersson JL, Auerbach EJ, Behrens TE, Coalson TS, Harms MP, Jenkinson M, Moeller S, Robinson EC, Sotiropoulos SN, Xu J, Yacoub E, Ugurbil K, Van Essen DC. The Human Connectome Project's neuroimaging approach. Nat Neurosci 2016;19(9):1175–1187. [PubMed: 27571196]

9. Setsompop K, Kimmlingen R, Eberlein E, Witzel T, Cohen-Adad J, McNab JA, Keil B, Tisdall MD, Hoecht P, Dietz P, Cauley SF, Tountcheva V, Matschl V, Lenz VH, Heberlein K, Potthast A, Thein H, Van Horn J, Toga A, Schmitt F, Lehne D, Rosen BR, Wedeen V, Wald LL. Pushing the limits of in vivo diffusion MRI for the Human Connectome Project. Neuroimage 2013;80:220–233. [PubMed: 23707579]
10. Van Essen DC, Ugurbil K. The future of the human connectome. Neuroimage 2012;62(2):1299–1310. [PubMed: 22245355]
11. Howell BR, Styner MA, Gao W, Yap PT, Wang L, Baluyot K, Yacoub E, Chen G, Potts T, Salzwedel A, Li G, Gilmore JH, Piven J, Smith JK, Shen D, Ugurbil K, Zhu H, Lin W, Elison JT. The UNC/UMN Baby Connectome Project (BCP): An overview of the study design and protocol development. Neuroimage 2019;185:891–905. [PubMed: 29578031]
12. Harms MP, Somerville LH, Ances BM, Andersson J, Barch DM, Bastiani M, Bookheimer SY, Brown TB, Buckner RL, Burgess GC, Coalson TS, Chappell MA, Dapretto M, Douaud G, Fischl B, Glasser MF, Greve DN, Hodge C, Jamison KW, Jbabdi S, Kandala S, Li X, Mair RW, Mangia S, Marcus D, Mascali D, Moeller S, Nichols TE, Robinson EC, Salat DH, Smith SM, Sotiropoulos SN, Terpstra M, Thomas KM, Tisdall MD, Ugurbil K, van der Kouwe A, Woods RP, Zollei L, Van Essen DC, Yacoub E. Extending the Human Connectome Project across ages: Imaging protocols for the Lifespan Development and Aging projects. Neuroimage 2018;183:972–984. [PubMed: 30261308]
13. Bookheimer SY, Salat DH, Terpstra M, Ances BM, Barch DM, Buckner RL, Burgess GC, Curtiss SW, Diaz-Santos M, Elam JS, Fischl B, Greve DN, Hagy HA, Harms MP, Hatch OM, Hedden T, Hodge C, Japardi KC, Kuhn TP, Ly TK, Smith SM, Somerville LH, Ugurbil K, van der Kouwe A, Van Essen D, Woods RP, Yacoub E. The Lifespan Human Connectome Project in Aging: An overview. Neuroimage 2019;185:335–348. [PubMed: 30332613]
14. Church GM. BRAIN: innovative neurotechnologies for imaging and therapeutics. Dialogues Clin Neurosci 2013;15(3):241–243. [PubMed: 24174897]
15. Leemans A Diffusion MRI of the brain: The naked truth. NMR Biomed 2019;32(4):e4084. [PubMed: 30791163]
16. Maier-Hein KH, Neher PF, Houde JC, Cote MA, Garyfallidis E, Zhong J, Chamberland M, Yeh FC, Lin YC, Ji Q, Reddick WE, Glass JO, Chen DQ, Feng Y, Gao C, Wu Y, Ma J, Renjie H, Li Q, Westin CF, Deslauriers-Gauthier S, Gonzalez JOO, Paquette M, St-Jean S, Girard G, Rheault F, Sidhu J, Tax CMW, Guo F, Mesri HY, David S, Froeling M, Heemskerk AM, Leemans A, Bore A, Pinsard B, Bedetti C, Desrosiers M, Brambati S, Doyon J, Sarica A, Vasta R, Cerasa A, Quattrone A, Yeatman J, Khan AR, Hodges W, Alexander S, Romascano D, Barakovic M, Auria A, Esteban O, Lemkaddem A, Thiran JP, Cetingul HE, Odry BL, Mailhe B, Nadar MS, Pizzagalli F, Prasad G, Villalon-Reina JE, Galvis J, Thompson PM, Requejo FS, Laguna PL, Lacerda LM, Barrett R, Dell'Acqua F, Catani M, Petit L, Caruyer E, Daducci A, Dyrby TB, Holland-Letz T, Hilgetag CC, Stieltjes B, Descoteaux M. The challenge of mapping the human connectome based on diffusion tractography. Nat Commun 2017;8(1):1349. [PubMed: 29116093]
17. Andersson JLR, Sotiropoulos SN. An integrated approach to correction for off-resonance effects and subject movement in diffusion MR imaging. Neuroimage 2016;125:1063–1078. [PubMed: 26481672]
18. Andersson JL, Skare S, Ashburner J. How to correct susceptibility distortions in spin-echo echo-planar images: application to diffusion tensor imaging. Neuroimage 2003;20(2):870–888. [PubMed: 14568458]
19. Holdsworth SJ, O'Halloran R, Setsompop K. The quest for high spatial resolution diffusion-weighted imaging of the human brain in vivo. NMR Biomed 2019;32(4):e4056. [PubMed: 30730591]
20. Engstrom M, Martensson M, Avventi E, Skare S. On the signal-to-noise ratio efficiency and slab-banding artifacts in three-dimensional multislab diffusion-weighted echo-planar imaging. Magn Reson Med 2015;73(2):718–725. [PubMed: 24647997]
21. Alexander DC, Dyrby TB, Nilsson M, Zhang H. Imaging brain microstructure with diffusion MRI: practicality and applications. NMR Biomed 2019;32(4):e3841. [PubMed: 29193413]

22. Engstrom M, Skare S. Diffusion-weighted 3D multislab echo planar imaging for high signal-to-noise ratio efficiency and isotropic image resolution. Magn Reson Med 2013;70(6):1507–1514. [PubMed: 23359357]
23. Rooney WD, Johnson G, Li X, Cohen ER, Kim SG, Ugurbil K, Springer CS, Jr. Magnetic field and tissue dependencies of human brain longitudinal 1H2O relaxation in vivo. Magn Reson Med 2007;57(2):308–318. [PubMed: 17260370]
24. Wu W, Poser BA, Douaud G, Frost R, In MH, Speck O, Koopmans PJ, Miller KL. High-resolution diffusion MRI at 7T using a three-dimensional multi-slab acquisition. Neuroimage 2016;143:1–14. [PubMed: 27570110]
25. Bruce IP, Chang HC, Petty C, Chen NK, Song AW. 3D-MB-MUSE: A robust 3D multi-slab, multiband and multi-shot reconstruction approach for ultrahigh resolution diffusion MRI. Neuroimage 2017;159:46–56. [PubMed: 28732674]
26. Holtrop JL, Sutton BP. High spatial resolution diffusion weighted imaging on clinical 3 T MRI scanners using multislab spiral acquisitions. J Med Imaging (Bellingham) 2016;3(2):023501. [PubMed: 27088107]
27. Eichner C, Setsompop K, Koopmans PJ, Lutzkendorf R, Norris DG, Turner R, Wald LL, Heidemann RM. Slice accelerated diffusion-weighted imaging at ultra-high field strength. Magn Reson Med 2014;71(4):1518–1525. [PubMed: 23798017]
28. Strotmann B, Heidemann RM, Anwander A, Weiss M, Trampel R, Villringer A, Turner R. High-resolution MRI and diffusion-weighted imaging of the human habenula at 7 tesla. J Magn Reson Imaging 2014;39(4):1018–1026. [PubMed: 24259421]
29. Chang HC, Sundman M, Petit L, Guhaniyogi S, Chu ML, Petty C, Song AW, Chen NK. Human brain diffusion tensor imaging at submillimeter isotropic resolution on a 3Tesla clinical MRI scanner. Neuroimage 2015;118:667–675. [PubMed: 26072250]
30. Jones DK, Alexander DC, Bowtell R, Cercignani M, Dell'Acqua F, McHugh DJ, Miller KL, Palombo M, Parker GJM, Rudrapatna US, Tax CMW. Microstructural imaging of the human brain with a 'super-scanner': 10 key advantages of ultra-strong gradients for diffusion MRI. Neuroimage 2018;182:8–38. [PubMed: 29793061]
31. Weiger M, Overweg J, Rosler MB, Froidevaux R, Hennel F, Wilm BJ, Penn A, Sturzenegger U, Schuth W, Mathlener M, Borgo M, Bornert P, Leussler C, Luechinger R, Dietrich BE, Reber J, Brunner DO, Schmid T, Vionnet L, Pruessmann KP. A high-performance gradient insert for rapid and short-T2 imaging at full duty cycle. Magn Reson Med 2018;79(6):3256–3266. [PubMed: 28983969]
32. Alsop DC, Connick TJ. Optimization of torque-balanced asymmetric head gradient coils. Magn Reson Med 1996;35(6):875–886. [PubMed: 8744016]
33. Chronik BA, Alejski A, Rutt BK. Design and fabrication of a three-axis edge ROU head and neck gradient coil. Magn Reson Med 2000;44(6):955–963. [PubMed: 11108634]
34. Foo TKF, Laskaris E, Vermilyea M, Xu M, Thompson P, Conte G, Epps C, Immer C, Lee SK, Tan ET, Graziani D, Mathieu JB, Hardy CJ, Schenck JF, Fiveland E, Stautner W, Ricci J, Piel J, Park K, Hua Y, Bai Y, Kagan A, Stanley D, Weavers PT, Gray E, Shu Y, Frick MA, Campeau NG, Trzasko J, Huston J, Bernstein MA. Lightweight, compact, and high-performance 3T MR system for imaging the brain and extremities. Magnetic Resonance in Medicine 2018;80(5):2232–2245. [PubMed: 29536587]
35. Davids M, Guerin B, Malzacher M, Schad LR, Wald LL. Predicting Magnetostimulation Thresholds in the Peripheral Nervous System using Realistic Body Models. Sci Rep 2017;7(1):5316. [PubMed: 28706244]
36. Wilm BJ, Pruessmann KP, et a. Diffusion MRI of the Brain with a Gradient Strength of 100 mT/m and a Slew Rate of 1200 T/m/s. Proc Intl Soc Mag Reson Med 2019:3504.
37. Choi S, Cunningham DT, Aguila F, Corrigan JD, Bogner J, Mysiw WJ, Knopp MV, Schmalbrock P. DTI at 7 and 3 T: systematic comparison of SNR and its influence on quantitative metrics. Magn Reson Imaging 2011;29(6):739–751. [PubMed: 21571473]
38. Wu X, Auerbach EJ, Vu AT, Moeller S, Lenglet C, Schmitter S, Van de Moortele PF, Yacoub E, Ugurbil K. High-resolution whole-brain diffusion MRI at 7T using radiofrequency parallel transmission. Magn Reson Med 2018;80(5):1857–1870. [PubMed: 29603381]

39. Reese TG, Heid O, Weisskoff RM, Wedeen VJ. Reduction of eddy-current-induced distortion in diffusion MRI using a twice-refocused spin echo. Magn Reson Med 2003;49(1):177–182. [PubMed: 12509835]
40. Andersson JL, Sotiropoulos SN. An integrated approach to correction for off-resonance effects and subject movement in diffusion MR imaging. Neuroimage 2016;125:1063–1078. [PubMed: 26481672]
41. Wilm BJ, Barmet C, Gross S, Kasper L, Vannesjo SJ, Haeberlin M, Dietrich BE, Brunner DO, Schmid T, Pruessmann KP. Single-shot spiral imaging enabled by an expanded encoding model: Demonstration in diffusion MRI. Magn Reson Med 2017;77(1):83–91. [PubMed: 27770473]
42. Wilm BJ, Barmet C, Pavan M, Pruessmann KP. Higher order reconstruction for MRI in the presence of spatiotemporal field perturbations. Magn Reson Med 2011;65(6):1690–1701. [PubMed: 21520269]
43. Sotiropoulos SN, Hernandez-Fernandez M, Vu AT, Andersson JL, Moeller S, Yacoub E, Lenglet C, Ugurbil K, Behrens TE, Jbabdi S. Fusion in diffusion MRI for improved fibre orientation estimation: An application to the 3T and 7T data of the Human Connectome Project. Neuroimage 2016;134:396–409. [PubMed: 27071694]
44. Gulban OF, De Martino F, Vu AT, Yacoub E, Ugurbil K, Lenglet C. Cortical fibers orientation mapping using in-vivo whole brain 7T diffusion MRI. Neuroimage 2018;178:104–118. [PubMed: 29753105]
45. Keil B, Blau JN, Biber S, Hoecht P, Tountcheva V, Setsompop K, Triantafyllou C, Wald LL. A 64-channel 3T array coil for accelerated brain MRI. Magn Reson Med 2013;70(1):248–258. [PubMed: 22851312]
46. Vaidya MV, Sodickson DK, Lattanzi R. Approaching Ultimate Intrinsic SNR in a Uniform Spherical Sample with Finite Arrays of Loop Coils. Concepts Magn Reson Part B Magn Reson Eng 2014;44(3):53–65. [PubMed: 26097442]
47. Wiggins GC, Polimeni JR, Potthast A, Schmitt M, Alagappan V, Wald LL. 96-Channel receive-only head coil for 3 Tesla: design optimization and evaluation. Magn Reson Med 2009;62(3):754–762. [PubMed: 19623621]
48. Pruessmann KP, Weiger M, Scheidegger MB, Boesiger P. SENSE: sensitivity encoding for fast MRI. Magn Reson Med 1999;42(5):952–962. [PubMed: 10542355]
49. Ugurbil K, Auerbach E, Moeller S, Grant A, Wu X, Van de Moortele PF, Olman C, DelaBarre L, Schillak S, Radder J, Lagore R, Adriany G. Brain imaging with improved acceleration and SNR at 7 Tesla obtained with 64-channel receive array. Magn Reson Med 2019;82(1):495–509. [PubMed: 30803023]
50. Ugurbil K Imaging at ultrahigh magnetic fields: History, challenges, and solutions. Neuroimage 2018;168:7–32. [PubMed: 28698108]
51. De Martino F, Yacoub E, Kemper V, Moerel M, Uludag K, De Weerd P, Ugurbil K, Goebel R, Formisano E. The impact of ultra-high field MRI on cognitive and computational neuroimaging. Neuroimage 2018;168:366–382. [PubMed: 28396293]
52. Dumoulin SO, Fracasso A, van der Zwaag W, Siero JCW, Petridou N. Ultra-high field MRI: Advancing systems neuroscience towards mesoscopic human brain function. Neuroimage 2018;168:345–357. [PubMed: 28093360]
53. Moeller S, Yacoub E, Olman CA, Auerbach E, Strupp J, Harel N, Ugurbil K. Multiband multislice GE-EPI at 7 tesla, with 16-fold acceleration using partial parallel imaging with application to high spatial and temporal whole-brain fMRI. Magn Reson Med 2010;63(5):1144–1153. [PubMed: 20432285]
54. Wiesinger F, Van de Moortele PF, Adriany G, De Zanche N, Ugurbil K, Pruessmann KP. Potential and feasibility of parallel MRI at high field. NMR Biomed 2006;19(3):368–378. [PubMed: 16705638]
55. Ohliger MA, Grant AK, Sodickson DK. Ultimate intrinsic signal-to-noise ratio for parallel MRI: electromagnetic field considerations. Magn Reson Med 2003;50(5):1018–1030. [PubMed: 14587013]
56. Barth M, Breuer F, Koopmans PJ, Norris DG, Poser BA. Simultaneous multislice (SMS) imaging techniques. Magn Reson Med 2016;75(1):63–81. [PubMed: 26308571]

57. Van de Moortele PF, Akgun C, Adriany G, Moeller S, Ritter J, Collins CM, Smith MB, Vaughan JT, Ugurbil K. B(1) destructive interferences and spatial phase patterns at 7 T with a head transceiver array coil. Magn Reson Med 2005;54(6):1503–1518. [PubMed: 16270333]
58. Yang QX, Wang J, Zhang X, Collins CM, Smith MB, Liu H, Zhu XH, Vaughan JT, Ugurbil K, Chen W. Analysis of wave behavior in lossy dielectric samples at high field. Magn Reson Med 2002;47(5):982–989. [PubMed: 11979578]
59. Guerin B, Setsompop K, Ye H, Poser BA, Stenger AV, Wald LL. Design of parallel transmission pulses for simultaneous multislice with explicit control for peak power and local specific absorption rate. Magn Reson Med 2015;73(5):1946–1953. [PubMed: 24938991]
60. Sharma A, Bammer R, Stenger VA, Grissom WA. Low peak power multiband spokes pulses for B1 (+) inhomogeneity-compensated simultaneous multislice excitation in high field MRI. Magn Reson Med 2015;74(3):747–755. [PubMed: 25203620]
61. Wu X, Tian J, Schmitter S, Vaughan JT, Ugurbil K, Van de Moortele PF. Distributing coil elements in three dimensions enhances parallel transmission multiband RF performance: A simulation study in the human brain at 7 Tesla. Magn Reson Med 2016;75(6):2464–2472. [PubMed: 26997332]
62. Koopmans PJ, Boyacioglu R, Barth M, Norris DG. Whole brain, high resolution spin-echo resting state fMRI using PINS multiplexing at 7 T. Neuroimage 2012;62(3):1939–1946. [PubMed: 22683385]
63. Wu X, Schmitter S, Auerbach EJ, Moeller S, Ugurbil K, Van de Moortele PF. Simultaneous multislice multiband parallel radiofrequency excitation with independent slice-specific transmit B1 homogenization. Magn Reson Med 2013;70(3):630–638. [PubMed: 23801410]
64. Poser BA, Anderson RJ, Guerin B, Setsompop K, Deng W, Mareyam A, Serano P, Wald LL, Stenger VA. Simultaneous multislice excitation by parallel transmission. Magn Reson Med 2014;71(4):1416–1427. [PubMed: 23716365]
65. Setsompop K, Gagoski BA, Polimeni JR, Witzel T, Wedeen VJ, Wald LL. Blipped-controlled aliasing in parallel imaging for simultaneous multislice Echo Planar Imaging with reduced g-factor penalty. Magn Reson Med 2012;67(5):1210–1224. [PubMed: 21858868]
66. Zahneisen B, Poser BA, Ernst T, Stenger VA. Three-dimensional Fourier encoding of simultaneously excited slices: generalized acquisition and reconstruction framework. Magn Reson Med 2014;71(6):2071–2081. [PubMed: 23878075]
67. Breuer FA, Kannengiesser SA, Blaimer M, Seiberlich N, Jakob PM, Griswold MA. General formulation for quantitative G-factor calculation in GRAPPA reconstructions. Magn Reson Med 2009;62(3):739–746. [PubMed: 19585608]
68. Xu J, Moeller S, Auerbach EJ, Strupp J, Smith SM, Feinberg DA, Yacoub E, Ugurbil K. Evaluation of slice accelerations using multiband echo planar imaging at 3 T. Neuroimage 2013;83:991–1001. [PubMed: 23899722]
69. Cauley SF, Polimeni JR, Bhat H, Wald LL, Setsompop K. Interslice leakage artifact reduction technique for simultaneous multislice acquisitions. Magn Reson Med 2014;72(1):93–102. [PubMed: 23963964]
70. Todd N, Moeller S, Auerbach EJ, Yacoub E, Flandin G, Weiskopf N. Evaluation of 2D multiband EPI imaging for high-resolution, whole-brain, task-based fMRI studies at 3T: Sensitivity and slice leakage artifacts. Neuroimage 2016;124(Pt A):32–42. [PubMed: 26341029]
71. Moeller S Simultaneous Multi-Slice Methods. ISMRM 2017:8111.
72. Liao C, Manhard MK, Bilgic B, Tian Q, Fan Q, Han S, Wang F, Park DJ, Witzel T, Zhong J, Wang H, Wald LL, Setsompop K. Phase-matched virtual coil reconstruction for highly accelerated diffusion echo-planar imaging. Neuroimage 2019;194:291–302. [PubMed: 30953837]
73. Chieh SW, Kaveh M, Akcakaya M, Moeller S. Self-calibrated interpolation of non-Cartesian data with GRAPPA in parallel imaging. Magn Reson Med 2019.
74. Knoll F, Hammernik K, Zhang C, Moeller S, Pock T, Sodickson DK, Akcakaya M. Deep-Learning Methods for Parallel Magnetic Resonance Imaging Reconstruction: A Survey of the Current Approaches, Trends, and Issues. IEEE Signal Processing Magazine 2020;37(1):128–140. [PubMed: 33758487]

75. Akcakaya M, Moeller S, Weingartner S, Ugurbil K. Scan-specific robust artificial-neural-networks for k-space interpolation (RAKI) reconstruction: Database-free deep learning for fast imaging. Magn Reson Med 2019;81(1):439–453. [PubMed: 30277269]
76. Chi Zhang SM, Sebastian Weingärtner, Kâmil Uğurbil, Mehmet Akçakaya. Accelerated MRI Using Residual RAKI: Scan-specific Learning of Reconstruction Artifacts. ISMRM 2019;2019:663.
77. Burhaneddin Yaman SAHH, Steen Moeller, Ellermann Jutta, Kâmil Uğurbil, Mehmet Akçakaya. Self-Supervised Learning of Physics-Based Reconstruction Neural Networks without Fully-Sampled Reference Data. ArXiv 2019;1912.07669.
78. Knoll F, Hammernik K, Zhang C, Moeller S, Pock T, Sodickson DK, Akcakaya M. Deep-Learning Methods for Parallel Magnetic Resonance Imaging Reconstruction: A Survey of the Current Approaches, Trends, and Issues. 2020;37(1):128–140.
79. Andersson JL, Sotiropoulos SN. Non-parametric representation and prediction of single- and multi-shell diffusion-weighted MRI data using Gaussian processes. Neuroimage 2015;122:166–176. [PubMed: 26236030]
80. Andersson JLR, Graham MS, Drobnjak I, Zhang H, Filippini N, Bastiani M. Towards a comprehensive framework for movement and distortion correction of diffusion MR images: Within volume movement. Neuroimage 2017;152:450–466. [PubMed: 28284799]
81. Barmet C, De Zanche N, Pruessmann KP. Spatiotemporal magnetic field monitoring for MR. Magn Reson Med 2008;60(1):187–197. [PubMed: 18581361]
82. Kasper L, Engel M, Barmet C, Haeberlin M, Wilm BJ, Dietrich BE, Schmid T, Gross S, Brunner DO, Stephan KE, Pruessmann KP. Rapid anatomical brain imaging using spiral acquisition and an expanded signal model. Neuroimage 2018;168:88–100. [PubMed: 28774650]
83. Aranovitch A, Haeberlin M, Gross S, Dietrich BE, Wilm BJ, Brunner DO, Schmid T, Luechinger R, Pruessmann KP. Prospective motion correction with NMR markers using only native sequence elements. Magn Reson Med 2018;79(4):2046–2056. [PubMed: 28840611]
84. Herbst M, Maclaren J, Weigel M, Korvink J, Hennig J, Zaitsev M. Prospective motion correction with continuous gradient updates in diffusion weighted imaging. Magn Reson Med 2012;67(2):326–338. [PubMed: 22161984]
85. Behrens TE, Woolrich MW, Jenkinson M, Johansen-Berg H, Nunes RG, Clare S, Matthews PM, Brady JM, Smith SM. Characterization and propagation of uncertainty in diffusion-weighted MR imaging. Magn Reson Med 2003;50(5):1077–1088. [PubMed: 14587019]
86. Jbabdi S, Sotiropoulos SN, Savio AM, Grana M, Behrens TE. Model-based analysis of multishell diffusion MR data for tractography: how to get over fitting problems. Magn Reson Med 2012;68(6):1846–1855. [PubMed: 22334356]
87. Farooq H, Xu J, Nam JW, Keefe DF, Yacoub E, Georgiou T, Lenglet C. Microstructure Imaging of Crossing (MIX) White Matter Fibers from diffusion MRI. Sci Rep 2016;6:38927. [PubMed: 27982056]
88. Alexander DC. A general framework for experiment design in diffusion MRI and its application in measuring direct tissue-microstructure features. Magn Reson Med 2008;60(2):439–448. [PubMed: 18666109]
89. O'Donnell LJ, Daducci A, Wassermann D, Lenglet C. Advances in computational and statistical diffusion MRI. NMR Biomed 2019;32(4):e3805. [PubMed: 29134716]
90. Sotiropoulos SN, Jbabdi S, Andersson JL, Woolrich MW, Ugurbil K, Behrens TE. RubiX: combining spatial resolutions for Bayesian inference of crossing fibers in diffusion MRI. IEEE Trans Med Imaging 2013;32(6):969–982. [PubMed: 23362247]
91. Pisharady PK, Sotiropoulos SN, Duarte-Carvajalino JM, Sapiro G, Lenglet C. Estimation of white matter fiber parameters from compressed multiresolution diffusion MRI using sparse Bayesian learning. Neuroimage 2018;167:488–503. [PubMed: 28669918]
92. Michailovich O, Rathi Y, Dolui S. Spatially regularized compressed sensing for high angular resolution diffusion imaging. IEEE Trans Med Imaging 2011;30(5):1100–1115. [PubMed: 21536524]
93. Ye C, Li X, Chen J. A deep network for tissue microstructure estimation using modified LSTM units. Med Image Anal 2019;55:49–64. [PubMed: 31022640]

94. Aliotta E, Nourzadeh H, Sanders J, Muller D, Ennis DB. Highly accelerated, model-free diffusion tensor MRI reconstruction using neural networks. Med Phys 2019;46(4):1581–1591. [PubMed: 30677141]
95. Lin Z, Gong T, Wang K, Li Z, He H, Tong Q, Yu F, Zhong J. Fast learning of fiber orientation distribution function for MR tractography using convolutional neural network. Med Phys 2019;46(7):3101–3116. [PubMed: 31009085]
96. Golkov V, Dosovitskiy A, Sperl JI, Menzel MI, Czisch M, Samann P, Brox T, Cremers D. q-Space Deep Learning: Twelve-Fold Shorter and Model-Free Diffusion MRI Scans. IEEE Trans Med Imaging 2016;35(5):1344–1351. [PubMed: 27071165]
97. Zhang Q, Coolen BF, Nederveen AJ, Strijkers GJ. Three-dimensional diffusion imaging with spiral encoded navigators from stimulated echoes (3D-DISPENSE). Magn Reson Med 2019;81(2):1052–1065. [PubMed: 30257041]
98. Chen NK, Guidon A, Chang HC, Song AW. A robust multi-shot scan strategy for high-resolution diffusion weighted MRI enabled by multiplexed sensitivity-encoding (MUSE). Neuroimage 2013;72:41–47. [PubMed: 23370063]
99. Truong TK, Guidon A. High-resolution multishot spiral diffusion tensor imaging with inherent correction of motion-induced phase errors. Magn Reson Med 2014;71(2):790–796. [PubMed: 23450457]
100. Saritas EU, Lee D, Cukur T, Shankaranarayanan A, Nishimura DG. Hadamard slice encoding for reduced-FOV diffusion-weighted imaging. Magn Reson Med 2014;72(5):1277–1290. [PubMed: 24265013]
101. Setsompop K, Fan Q, Stockmann J, Bilgic B, Huang S, Cauley SF, Nummenmaa A, Wang F, Rathi Y, Witzel T, Wald LL. High-resolution in vivo diffusion imaging of the human brain with generalized slice dithered enhanced resolution: Simultaneous multislice (gSlider-SMS). Magn Reson Med 2017.
102. Moeller S, Van de Moortele PF, Goerke U, Adriany G, Ugurbil K. Application of parallel imaging to fMRI at 7 Tesla utilizing a high 1D reduction factor. Magn Reson Med 2006;56(1):118–129. [PubMed: 16767760]
103. Glover GH. Spiral imaging in fMRI. Neuroimage 2012;62(2):706–712. [PubMed: 22036995]
104. Block KT, Frahm J. Spiral imaging: a critical appraisal. J Magn Reson Imaging 2005;21(6):657–668. [PubMed: 15906329]
105. Vannesjo SJ, Graedel NN, Kasper L, Gross S, Busch J, Haeberlin M, Barmet C, Pruessmann KP. Image reconstruction using a gradient impulse response model for trajectory prediction. Magn Reson Med 2016;76(1):45–58. [PubMed: 26211410]
106. Duyn JH, Yang Y, Frank JA, van der Veen JW. Simple correction method for k-space trajectory deviations in MRI. J Magn Reson 1998;132(1):150–153. [PubMed: 9615415]
107. Robison RK, Li Z, Wang D, Ooi MB, Pipe JG. Correction of B0 eddy current effects in spiral MRI. Magn Reson Med 2019;81(4):2501–2513. [PubMed: 30444004]
108. Testud F, Gallichan D, Layton KJ, Barmet C, Welz AM, Dewdney A, Cocosco CA, Pruessmann KP, Hennig J, Zaitsev M. Single-shot imaging with higher-dimensional encoding using magnetic field monitoring and concomitant field correction. Magn Reson Med 2015;73(3):1340–1357. [PubMed: 24687529]
109. Veraart J, Novikov DS, Christiaens D, Ades-Aron B, Sijbers J, Fieremans E. Denoising of diffusion MRI using random matrix theory. Neuroimage 2016;142:394–406. [PubMed: 27523449]
110. Moeller S, Ramanna S, Lenglet C, Pisharady P, Auerbach E, Delabarre L, Wu X, Akcakaya M, Ugurbil K. Self navigation for 3D multi-shot EPI with data-reference. Magn Reson Med 2020;DOI: 10.1002/mrm.28231.

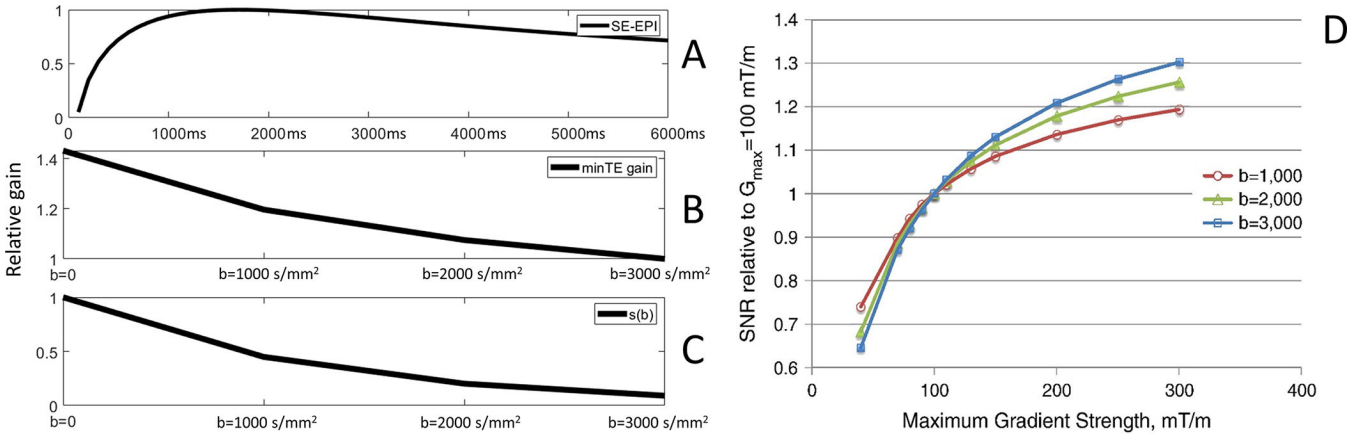

Figure 1:

Summary of performance metrics for the HCP scan evaluation for a T_1=1200ms. (A) The SNR efficiency, defined as SNR/√TR, as a function of TR. (B) The relative loss in SNR per shell by using the TE for the highest b value shell for all shells instead of the minimum TE for each b value. (C) The reduction in signal for different shells for isotropic diffusion with a diffusivity of 0.0017 mm^2/s for white matter representative of the corpus callosum. (D) SNR gain for different maximal gradient strength, and infinitely fast slew-rate.

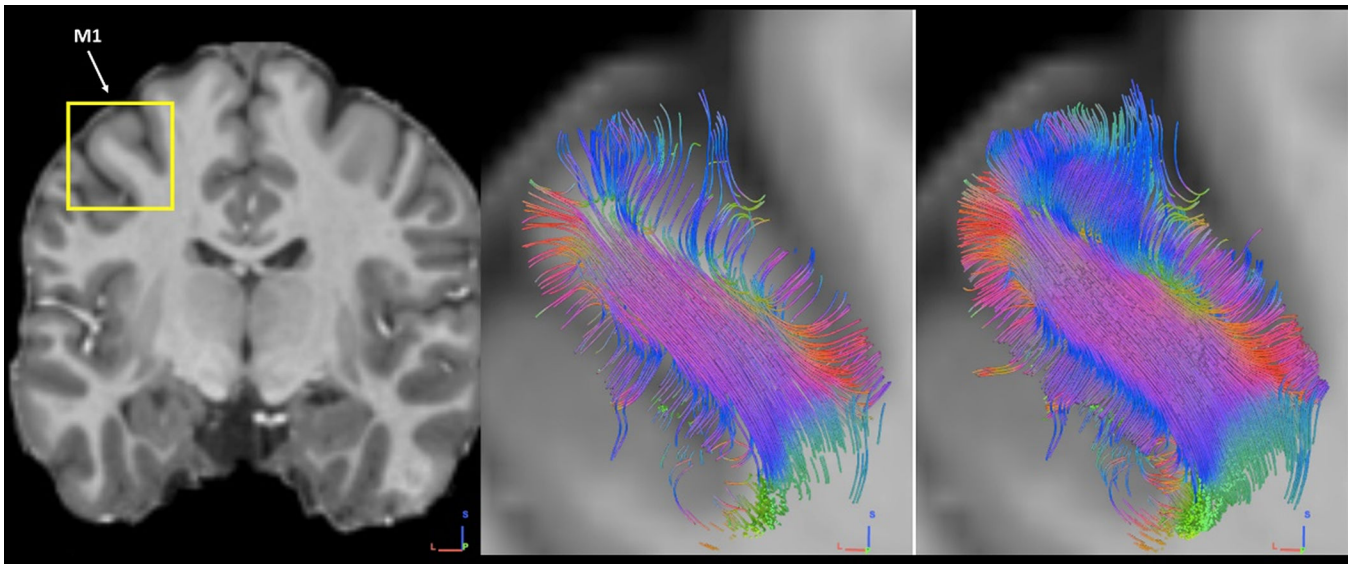

Figure 2:

7T Tractography (Euler integration using Gaussian radial basis functions for orientation interpolation with 10,000 streamlines) from the primary fiber orientation in the primary motor cortical area. Center image shows 1000 streamlines and right image shows 5000 streamlines to elucidate different levels of details in the display of the fiber distribution. Background image is unbiased T1-weighted data.

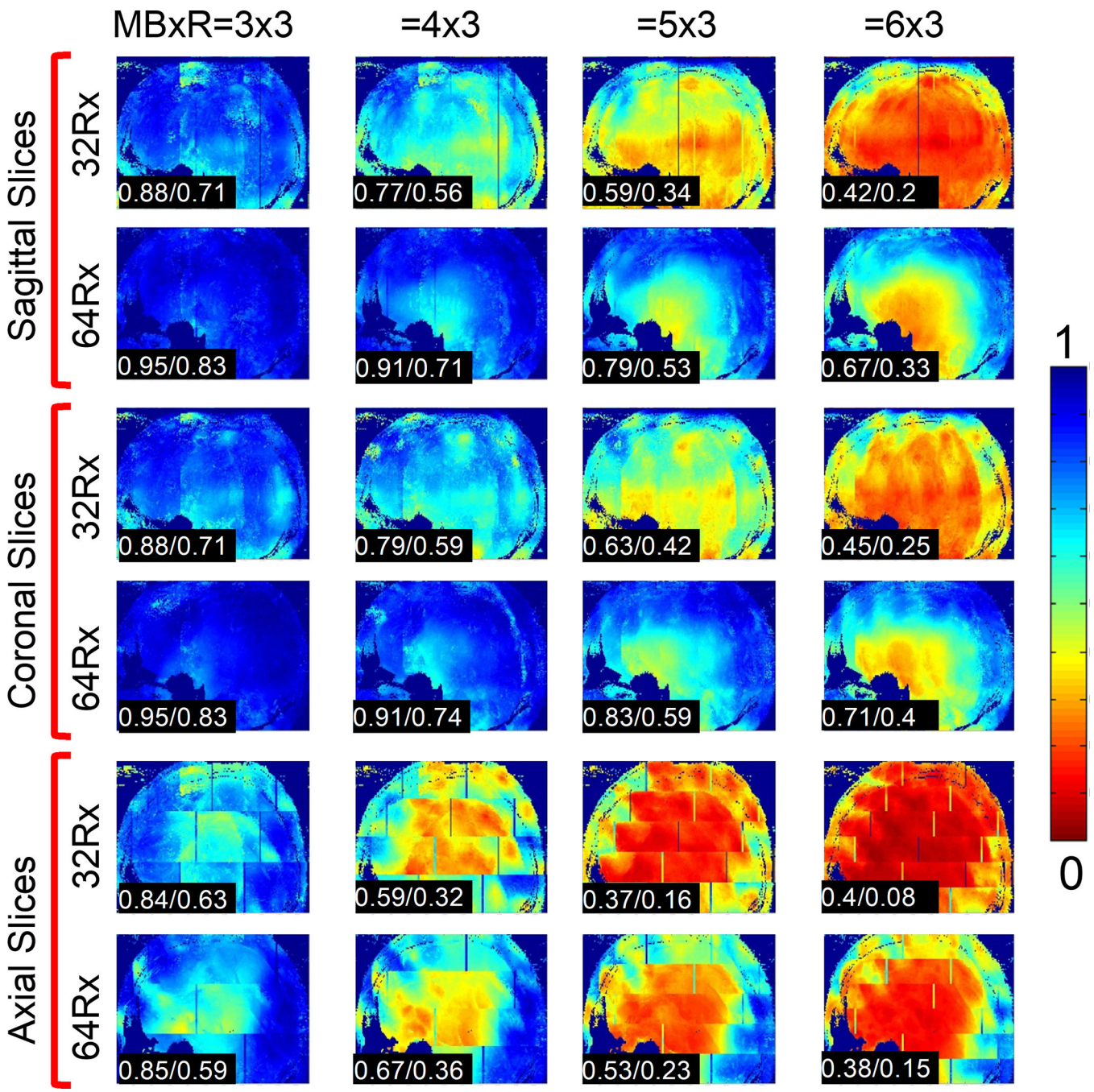

Figure 3:

1/g maps for SMS/MB acceleration for different MB factors for simultaneously excited slices with R = 3 in the phase encode dimension. The g-factor calculations are performed for sagittal, coronal, and axial slices and slice accelerations (labeled on the left side of the figure) with k-space undersampling performed on the AP direction for sagittal and axial slices and in the LR direction for the axial slices. The data are presented as a MIP over an 80-mm sagittal slab superimposed on a silhouette of a sagittal slice. The mean and the maximal (at 98% level) g-factor numbers are given as 1/g values in the lower left corner

for each figure. Images are from a representative subject, and numbers are averages over all participants. From (49)

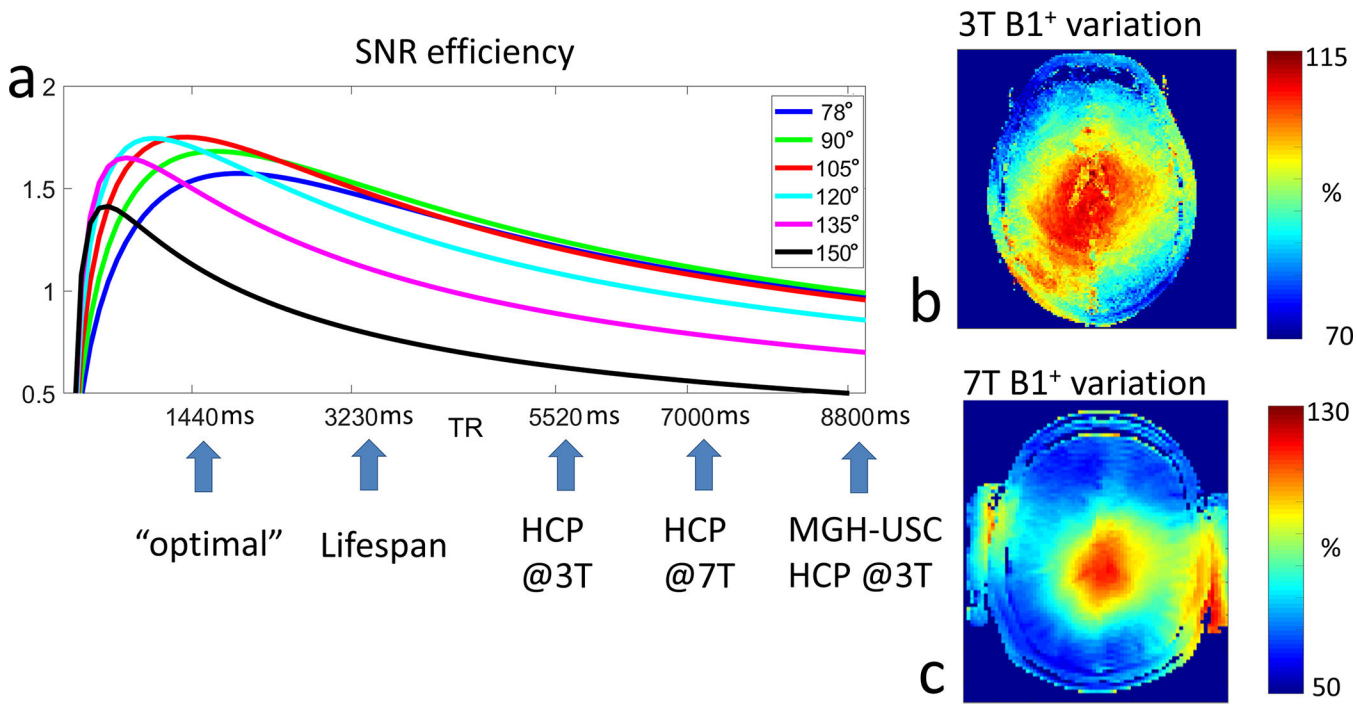

Figure 4:

a) SNR efficiency for different TRs and for different excitation flip angles for spins that have a T_1 of 1200ms relative to the SNR for TR=8800ms with a 180° refocusing pulse. (b), and (c) relative spatial variation of the flip angle at 3T (b) and 7T (c). The 7T used 5 mm thick, high permittivity dielectric pads under the neck and on both sides of the head to improve the normally poor B_1^+ in the cerebellum and temporal lobes and the pads are visible in the B_1^+ map, on each side of the axial slice shown.

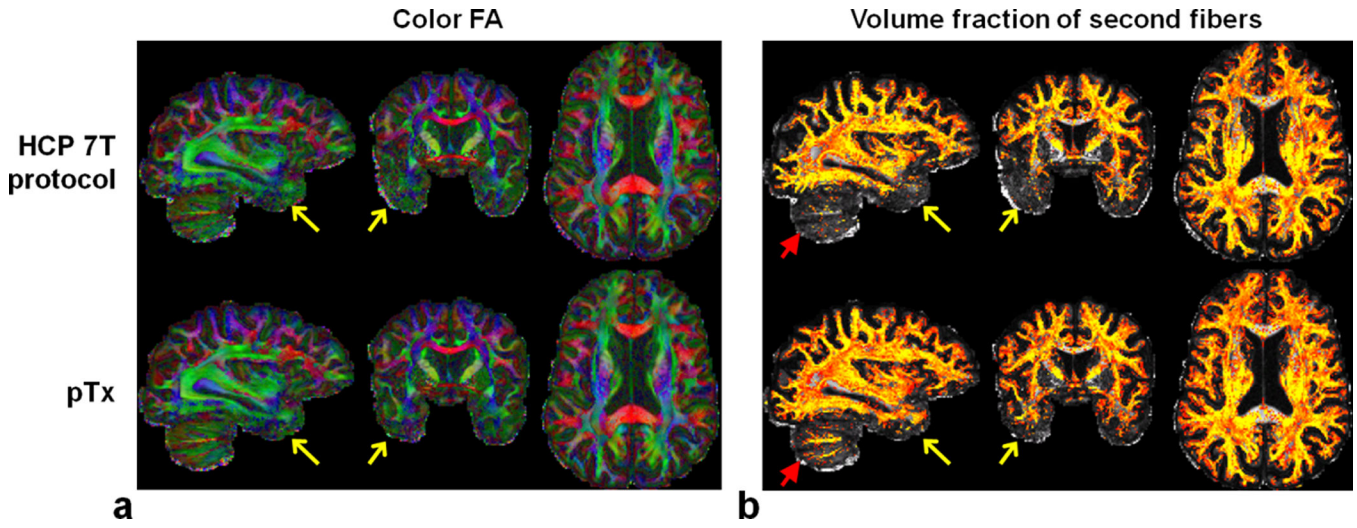

Figure 5:

Comparing HCP 7T dMRI protocol (HCP 1Tx) with the HCP protocol run with pTx pulses (HCP pTx protocol). Data are shown for one subject. Fractional anisotropy (FA) maps (left panel) and volume fraction maps for second fiber orientations (right panel). The color FA is FA (in the range of [0 1]) with the color representing the orientation of the principal fiber (red: left-right; green: A-P; blue: inferior-superior). The volume fraction map is shown in a colorscale of [0.05 0.2] (with yellow being high and red being low in volume fraction), overlaid on the respective FA map (in a grayscale of [0 1]). Both dMRI datasets were acquired with 1.05 mm isotropic resolutions, MB2, in-plane acceleration factor = 3, and TE = 71 ms. The TR for pTx acquisition was slightly longer (7400 versus 7000 ms). Both acquisitions used the same q-space sampling scheme (double shells, b-value = 1000/2000 s/mm^2), corresponding to 143 unique image volumes, each acquired twice with anterior-posterior (AP) and PA phase encode directions. Total scan time was kept constant for both datasets (i.e., 40 min divided into 4 segments of 10 min each). Note that the use of pTx improved fiber orientation estimation performances not only in lower temporal lobe (as indicated by yellow arrows) but also in cerebellum (as highlighted by red arrows). Adapted from (38).

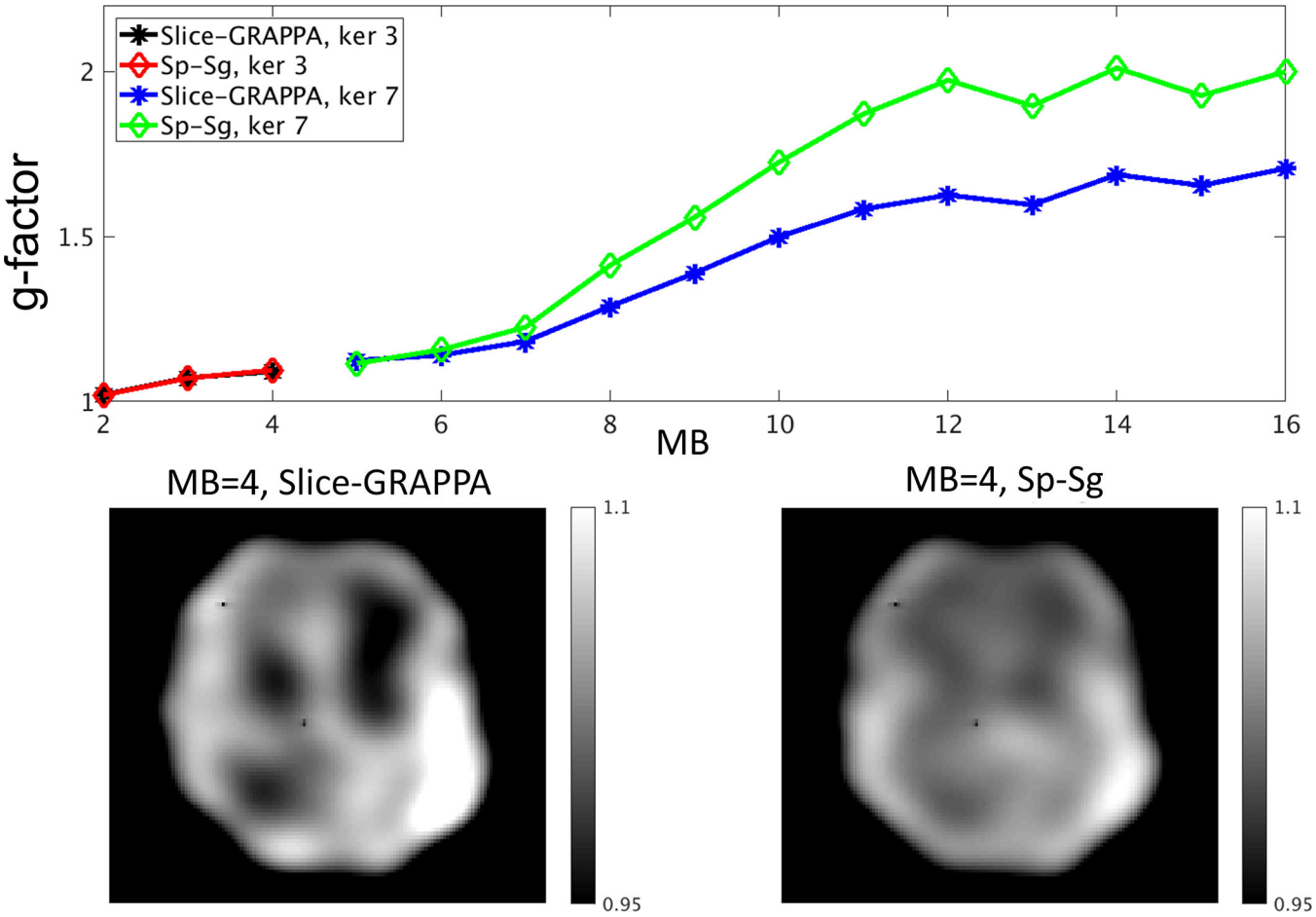

Figure 6:

Simulated maximal g-factor for SMS/MB 2D SE-EPI for Sp-Sg and slice-GRAPPA. Top; maximal g-factors using 99 percentile over a whole-brain acquisition as a function of the MB factor. For MB=[2,3,4] a kernel of 3×3 is used; for these MB factors the results are plotted using red and black colors, for Sp-Sg and slice GRAPPA, respectively, and they superimpose. For MB ≥4, a kernel of 7×7 is used; for these MB factors, the results are plotted in green and blue for Sp-Sg and slice GRAPPA, respectively. Bottom row, left, g-factor map using kernels calculated with Slice-GRAPPA, and bottom row right, g-factor map using kernels calculated with Sp-Sg.

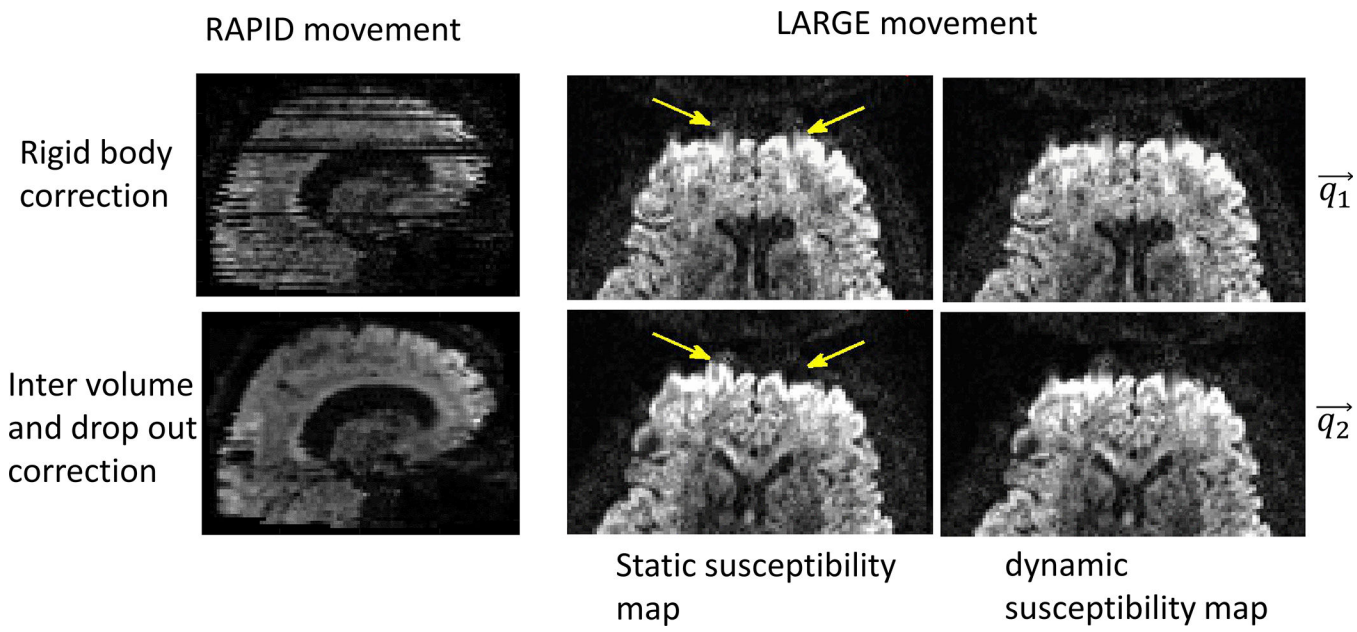

Figure 7.

Comparison of anatomical consistency with different model options in EDDY. Left column, the effect of spin-history in the presence of rapid movement, with a rigid body correction (top) and with an estimation for inter volume signal drop (bottom). Under large movement, and after correction, the corrected brain from different q-vectors should have the same brain outline. The static susceptibility map shows difference in the frontal areas (center column) as indicated with yellow arrows, and these are corrected using the dynamic susceptibility map (right most column). Adapted from https://fsl.fmrib.ox.ac.uk/fsl/fslwiki/eddy

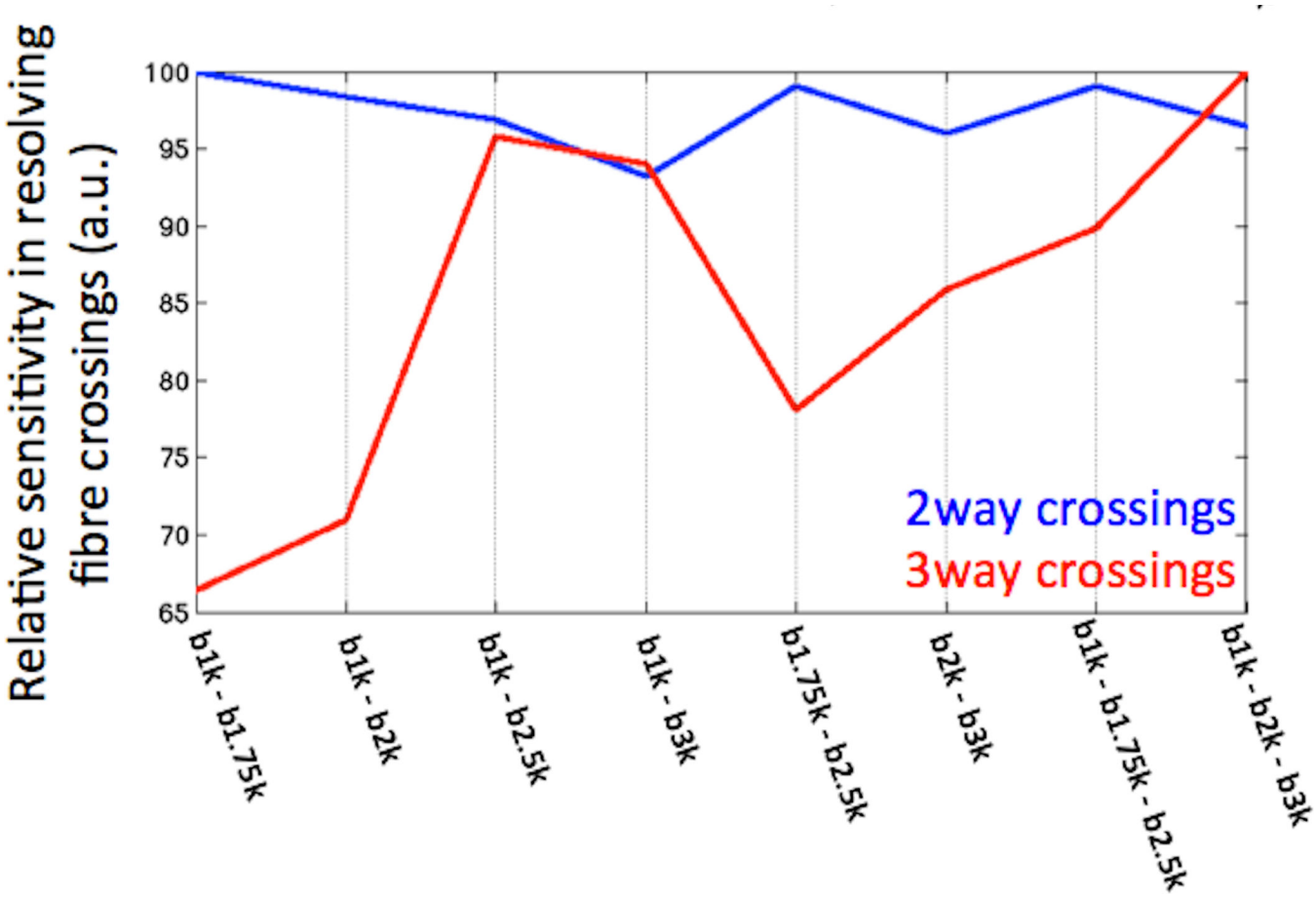

Figure 8.

Sensitivity of different *q*-space sampling schemes in resolving (two and three-way) crossing fibers within the centrum semiovale. The amount of crossings resolved by each scheme is normalized by the maximum. (6)

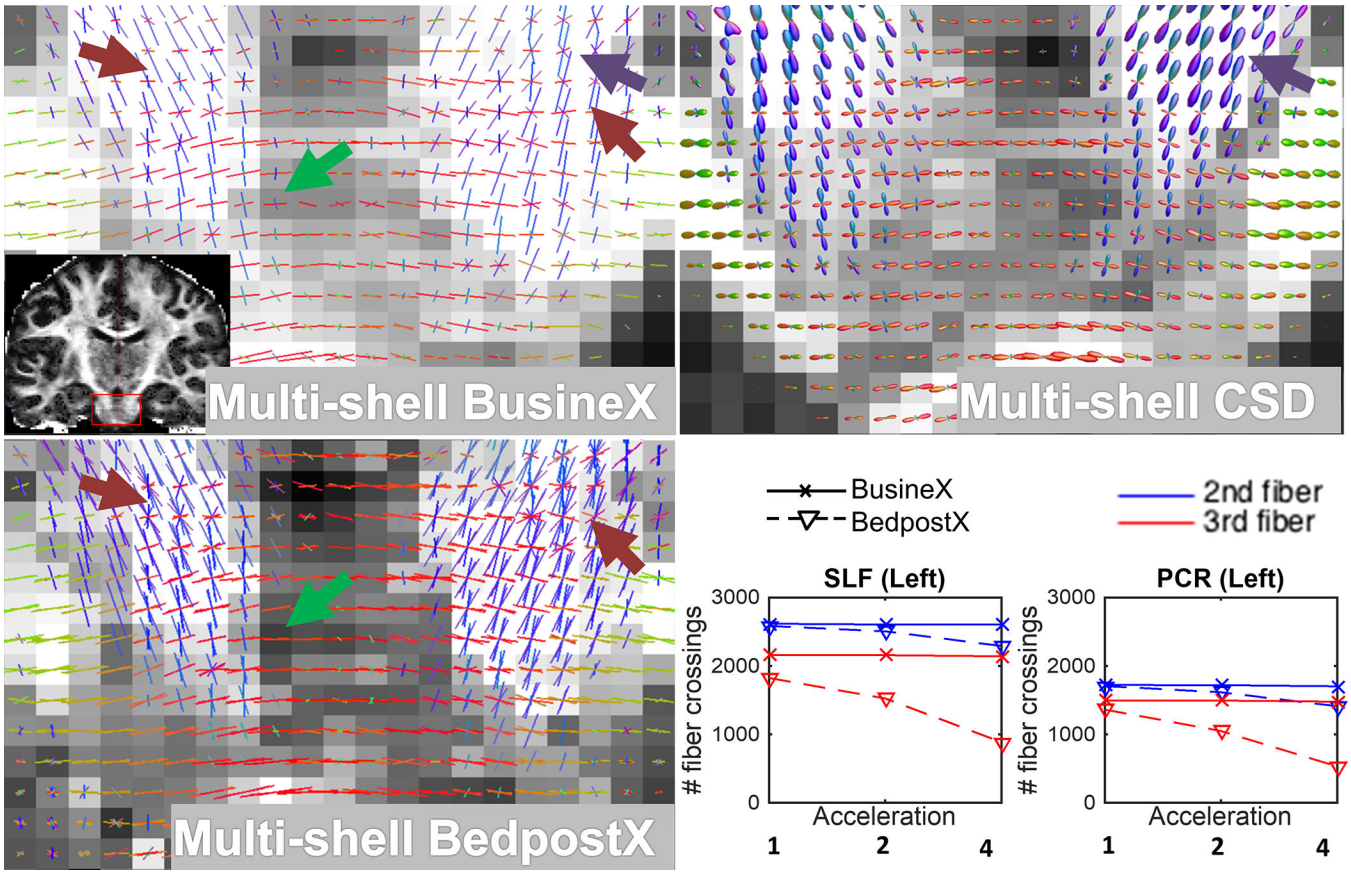

Figure 9:

Comparison between BusineX, BedpostX, and Constrained Spherical Deconvolution (CSD), showing improved fiber parameter estimations by BusineX. Upper panels and lower-left panel show color coded orientation estimates (orientation distribution functions in the case of CSD) at the pons region highlighted in the inset view. The background is the sum of anisotropic volume fractions for BusineX and BedpostX, and fractional anisotropy (FA) for the CSD. The areas highlighted with arrows depict the improvements; the better detection of fiber crossings (violet and green arrows) and the lower estimation uncertainty (red arrows). Lower right panel shows the detected number of second (blue) and third (red) fiber crossings at two representative ROIs (left superior longitudinal fasciculus and posterior corona radiata), and its variation with acceleration in diffusion gradient directions (under-sampling factor). The improved estimations in BusineX is due to the data-dependent local learning of hyperparameters, at each voxel and for each possible fiber orientation, that moderate the strength of priors governing the parameter variances.

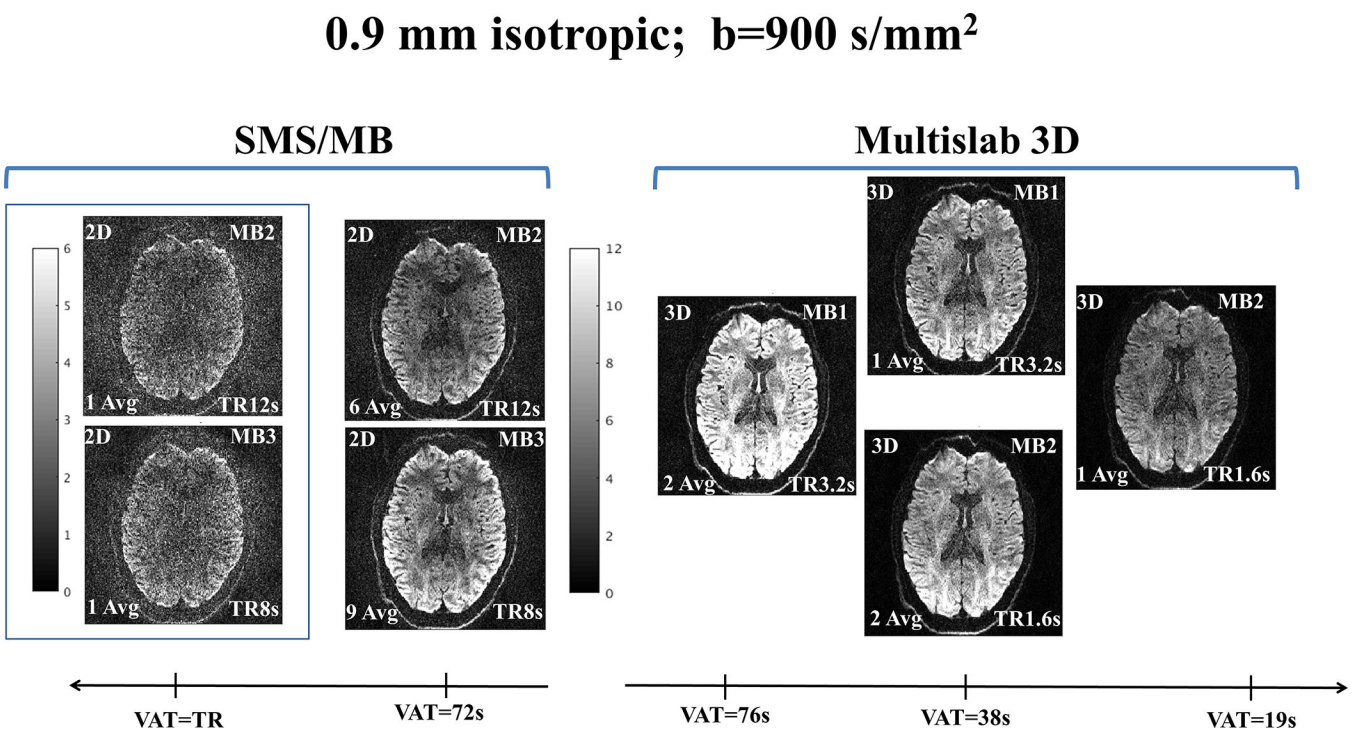

Figure 10:

Comparison of experimental SNR between 2 SMS/MB and 3D (Multislab-Multiband) high resolution acquisitions for whole brain, 0.9 mm isotropic resolution (reproduced from (110)), showing the SNR from the shortest VAT with what is feasible with 2D SMS/MB and 3D acquisitions with 8 slices/slab, all obtained with iPAT=2 to maintain a TE<100ms. The experimental thermal noise ($g \cdot \sigma$) is used as the hardware thermal noise, with g the encoding noise amplification and σ the system thermal noise. The 2D SMS with MB 2, 12s TR and 6 average (VAT=72s) is similar to the achievable SNR to a 3D acquisition using a TR=1.6s, 1 Average (VAT=19s). For approximately matched scan times of 72 s for SMS/MB and 76 s for 3D, the latter has 2x higher SNR. For matched scan-time the 3D with TR=1.6 s and 2 averages versus TR=3.2s and single average have similar SNR reflecting how the fact that SNR efficiency varies slowly near the optimal TR (Figure 3).

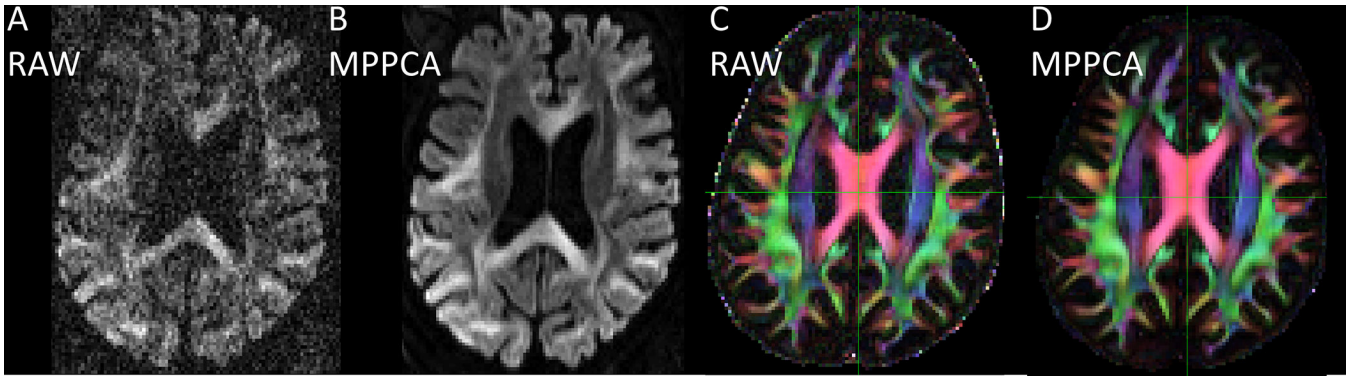

Figure 11:

The effect of MPPCA pre-processing on Life-span data. The MPPCA is applied to un-processed dMRI data. A slice from a volume with b=3000 s/mm^2 is show in A/ and the same slice after MPPCA noise variance reduction is shown in B. After post-processing as described in the “Preprocessing pipelines” the FA is calculated with FSL, and reproduced in C/ and D/ for the native DICOM and the MPPCA processed data respectively.

Table 1.

dMRI protocols for Human Connectome Projects

	3T MGH-USC HCP*	**3T WU-Minn HCP**	**7T WU-Minn HCP**	**3T LifeSpan HCP**
TR/TE (ms)	8800 / 57	5520 / 89.5	7000 / 71.2	3230 / 92.8
Resolution	1.5 mm isotropic	1.25 mm isotropic	1.05 mm isotropic	1.5 mm isotropic
Acceleration§, R/MB	3 / 1	1 / 3	3 / 2	4 / 1
Δ/δ (ms)	21.8/12.9	43/10.6	34/14.3	43.4/13.7
Phase Partial Fourier	6/8	6/8	6/8	6/8
Acquisition Time, min	89 min	60 min	40 min	21
Shells s/mm^2	1000, 3000, 5000, 10,000	1000, 2000, 3000	1000, 2000	1500, 3000

*The MGH-USC consortium data is from (https://www.humanconnectome.org/study/hcp-young-adult/document/mgh-adult-diffusion-data-acquisition-details)

§R is the reduction factor in the phase encode direction. MB is the multiband factor designating the number of simultaneously excited slices

Table 2:

SNR efficiency comparison between EPI and spiral acquisition across 3 different resolution for matched TR and T_2=65ms. For each resolution, R designates the amount of necessary EPI phase-encoding undersampling. For the Cartesian acquisition, the achievable echo spacing (ESP), echo time (TE) and echo train length (ETL) for b=3000 s/mm^2 are listed. The maximal TE gain, as the achievable gain feasible with a spiral acquisition, and the SNR gain from the shortened TE are listed. Gain from a spiral acquisition with an ADC (the spiral equivalent of ETL) of 80ms, feasible at 3T, relative to the EPI is listed rightmost and are in alignment with experimental validation reported in (26).

Resolution (mm)	R	Cartesian			TE gain (ms) for Spiral	SNR gain from (TE)	SNR gain From ADC
		ESP(us)	TE (ms)	ETL(ms)			
1.5	1	690	89.2	72.8	18.1	1.32	1.05
1.17	2	770	77.8	50.6	13	1.22	1.25
0.9	2	940	95.4	80.9	20.68	1.37	0.99